Progress In Electromagnetics Research, Vol. 173, 93–127, 2022

Spoof Surface Plasmons Arising from Corrugated Metal Surface to Structural Dispersion Waveguide

Liangliang Liu* and Zhuo Li*

Abstract—Metamaterials offer great promise for engineering electromagnetic properties beyond the limits of natural materials. A typical example is the so-called spoof surface plasmons (SPs), which mimic features of optical SPs without penetrating metal at lower frequencies. Spoof SPs inherit most of the properties of natural SPs, including dispersion characteristics, field confinement, localized resonance, and subwavelength resolution, and therefore are highly expected to offer a new solution for low-frequency applications. With the development of spoof SPs, three different theories have been introduced. The first one is the description of subwavelength corrugated metal surfaces by a metamaterial that hosts an effective plasma frequency. The second one is developed with high-index contrast grating, which can realize propagation with ultra low loss and localization with ultrahigh Q-factor resonance. The last one is structural dispersion induced SPs, a perfect low-frequency analogue of optical SPs, realized by exploiting the well-known structural dispersion waveguide modes only with positive-ε materials. Here, the developments of these three theories including propagation and localized SPs are reviewed, focusing primarily on the fundamental and representative applications.

1. INTRODUCTION

Plasmonics, a name coined for surface plasmons (SPs) related photonics, has inspired booming research interests since the late 1990s [1]. The history of SPs research dates back to the investigation of surface plasmon resonance (SPR) on metallic thin films [2], or even light scattering from nanoscale metallic particles as early as the 1970s [3]. SPs arise from the interaction between electromagnetic (EM) fields and the conduction electrons in a metal [1]. Conduction electrons can be driven by an EM field, which causes them to oscillate collectively. These charge density oscillations can be sustained within the bulk of metal as well as confined at the interface between a metal and a dielectric medium, in each case at a distinct resonance frequency. Spatially confined plasmon modes at metal/dielectric interfaces, i.e., SPs, are the subject of plasmonics research [4]. The fact that SPs are collective excitations of photons and electrons gives rise to a major characteristic: the subwavelength nature of SPs enables a strong localization and enhancement of the EM fields in the vicinity of metal/dielectricinterfaces [5–7]. As we describe below, two kinds of SPs exist, depending on the geometry of the interface under consideration. First, corrugated metal surfaces support the propagation of surface plasmon polaritons (SPPs), EM modes that propagate along the surface while featuring subwavelength confinement to it. Many research efforts have been devoted to the implementation of SPP-based photonics [5, 6], as metal structures can be designed to efficiently guide SPPs by, for instance, confining them in the transverse direction in one-dimensional (1D) plasmonic waveguides [8, 9]. Moreover, SPPs build a bridge between photonics and electronics, opening up the possibility of achieving more compact devices [10]. On the other hand, metal particles of dimensions smaller than the wavelength sustain confined SP modes at

Received 13 January 2022, Accepted 3 April 2022, Scheduled 18 April 2022

* Corresponding author: Liangliang Liu (lliu@nuaa.edu.cn), Zhuo Li (lizhuo@nuaa.edu.cn).

The authors are with the Key Laboratory of Radar Imaging and Microwave Photonics, Ministry of Education, College of Electronic and Information Engineering, Nanjing University of Aeronautics and Astronautics, Nanjing 211106, China.

optical frequencies, the so-called localized surface plasmons (LSPs). These are collective oscillations of the conduction electrons that give rise to subwavelength localization of the EM fields. LSPs in metal nanoparticles enable an efficient transfer of energy between then near- and far-fields, and for this reason, metal nanoparticles are considered as nano-antennas, the analogue of radio antennas but at higher frequencies [11–14]. Recently, SPs have been widely developed in many fields, including miniaturization of photonic circuits in terms of SPPs- and LSPs-based near field optics, surface-enhanced spectroscopy, plasmonic antennas, and photovoltaics [9–15]. In addition, they have been expected to bring important improvements in biosensing [16, 17], microscopy [18], extraordinary optical transmissions [19, 20], EM induced transparency [21, 22], etc. However, large dissipative losses severely limit the performance of metallic SPs-based devices, and the fact that metal surfaces sustain these confined EM modes only at visible wavelength prevents the transfer of plasmonic capabilities to lower frequency range, such as the microwave and terahertz (THz) regimes, where metals behave like perfect electric conductors (PECs). Nevertheless, it would be highly desirable to transfer the SP ability to confine light in deep subwavelength dimensions from the visible to lower frequencies.

It has been known that the addition of a subwavelength corrugation (i.e., arrays of holes) to a metal surface produces an enhanced surface impedance since the middle of the last century. This mechanism allows a surface mode bounded to the interface, even in the limit of PECs [23, 24], and is the origin of the frequency selective surfaces [25]. This effect can be understood by considering the presence of a periodic array of small holes within a perturbation method. Therefore, the dispersion relation of the surface EM modes maintained by the corrugated structure will follow the flat SPP (Zenneck or Sommerfeld surface waves [26, 27]), apart from the values close to the Brillouin zone boundary. Thus, the lowest band of the surface EM modes separates from the light line, binding the EM field more strongly to the surface as a result of the band bending caused by periodical holes [28]. The dispersion relation under the first gap represents a truly bounded surface mode. In 2004, Pendry et al. [29] proposed the concept of spoof SPPs, which mimic the exciting properties of optical SPPs at low frequencies by decorating the metal surface with periodic subwavelength holes or grooves. Importantly, different from their optical counterparts, spoof SPPs have a purely geometric origin. The corrugations on metal surfaces play the role of field penetration of real SPPs, and the geometrical parameters of corrugations determine the effective plasma frequency in the Drude model that leads to the dispersion of spoof SPPs [29, 30]. This elegant analogy between spoof SPPs on corrugated metal surfaces and SPPs has successfully resolved a long-standing debate on the role of SPPs in the extraordinary optical transmission through subwavelength holes [19, 29]. Aside from the propagating spoof SPPs, Pors et al. [31] demonstrated that periodically textured metallic particles in two and three dimensions can support spoof LSPs at low frequencies. Spoof LSPs are highly sensitive to the geometry of the metallic structures and the local dielectric environments and therefore have great potential applications in sensing, precision microscopy, high-resolution imaging, etc. These two spoof plasmonic metamaterials set up the basis for transferring the exotic features of optical SPPs and LSPs to lower frequencies and arouse a series of efforts to realize low-frequency surface plasmonics and their real applications.

In this work, the development of spoof surface plasmons (including SPPs and LSPs) arising in corrugated metallic surfaces, high-index contrast grating, and structural dispersion waveguide in recent years is reviewed, focusing primarily on the basic concept, theory, design method, efficient experiment implementation, and their real applications. The physical mechanism behind coupled-mode formalism and effective metamaterial approximation of these three low-frequency surface plasmons has been mainly revisited, and recent advances are reviewed accordingly. Finally, the future directions and potential applications of these spoof surface plasmons are discussed.

2. SPOOF SURFACE PLASMONS ARISING IN SUBWAVELENGTH METALLIC PERIODIC STRUCTURES

2.1. MGs-Induced Spoof SPPs

The early studies of plasmonic metamaterials mainly focused on the design, implementation, and characterization of effective EM parameters [32]. When it comes to spoof SPPs on corrugated metal surfaces as a new class of plasmonic metamaterials [30], it is reasonable to analyze their SPP-like dispersion from the perspective of the equivalent metamaterial models. Most importantly, it provides the

possibility of tailoring the dispersion relation of these spoof SPP modes by simply tuning the geometrical parameters of corrugations. As follows, we will review the deep physical insight into the effect that the orientation of the supporting structure has on the dispersion properties and field confinement features of these metallic gratings (MGs) induced surface EM waves.

2.1.1. Fundamental of MGs-Induced Spoof SPPs

As shown in Fig. 2(a), the first proposed structure of a 2D array of holes perforated on a PEC surface is given to support the propagation of the spoof SPP waves. Fig. 2(b) plots the corresponding dispersion relation, which exhibits a similar feature to that of optical SPPs as the dispersion curve is slightly below the light line at low frequencies, then deviates from the light line at higher frequencies, and finally reaches an asymptotic surface plasma frequency. To fully understand this designer surface EM mode, the dispersion relation in the limit of $k_{||}a \ll 1$ can be analytically derived as [29]

$$\frac{\sqrt{k_{||}^2 - k_0^2}}{k_0} = \frac{8a^2}{\pi^2 d^2} \frac{k_0}{\sqrt{\pi^2 d^2 - \varepsilon_h k_0^2}}, \tag{1}$$

where a and d are the side length and periodicity of the holes array; ε_h is the permittivity of the material filling the holes; $k_0 = \omega/c_0$ is the wave vector in free space (c_0 is the speed of light); and $k_{||}$ is the wave vector of surface waves propagating along the x-direction. From another point of view, the metallic surface with subwavelength decorations can be considered as an effective medium with effective permittivity and permeability in the x-y plane and infinite permittivity and permeability in the z-direction. The same dispersion curve has been obtained with the following effective components [29]

$$\left[\overline{\overline{\varepsilon}}\right] = \begin{bmatrix} \dfrac{\pi^2 d^2 \varepsilon_h}{8a^2}\left(1 - \dfrac{\omega_p^2}{\omega^2}\right) & 0 & 0 \\ 0 & \dfrac{\pi^2 d^2 \varepsilon_h}{8a^2}\left(1 - \dfrac{\omega_p^2}{\omega^2}\right) & 0 \\ 0 & 0 & \infty \end{bmatrix}, \quad \left[\overline{\overline{\mu}}\right] = \begin{bmatrix} \dfrac{8a^2\mu_h}{\pi^2 d^2} & 0 & 0 \\ 0 & \dfrac{8a^2\mu_h}{\pi^2 d^2} & 0 \\ 0 & 0 & \infty \end{bmatrix}. \tag{2}$$

where $\omega_p = \pi c_0/\sqrt{\varepsilon_h \mu_h}$ is regarded as the effective plasma frequency, which is the same as the cutoff frequency of the fundamental mode in the rectangle waveguide. For $\omega < \omega_p$, Equation (2) gives $\overline{\overline{\varepsilon}}_x = \overline{\overline{\varepsilon}}_y < 0$ in the effective media, which suggests that the proposed waveguide can support the designed surface plasmon modes. When $\omega > \omega_p$, the EM fields can propagate in the z-direction along the infinitely long holes. The PEC surface cannot sustain the EM energy-transportation along the x-direction, and the metal structure can be treated as a dielectric with $\overline{\overline{\varepsilon}}_x = \overline{\overline{\varepsilon}}_y > 0$. Moreover, if the holes are with finite depth and a PEC wall at the bottom, this waveguide structure can be equivalent to the air-dielectric-PEC sandwich structure, where the surface at the bottom plane can be treated as a PEC mirror. In this case, it may support a kind of guided mode similar to that in the air-dielectric-air waveguide. In view of these, the spoof SPP structures are also referred to as plasmonic metamaterials. This spoof SPP mode was first experimentally demonstrated in the microwave region on a conducting surface perforated with a 2D array of holes [33–36], as shown in Figs. 1(e) and 1(f). The grating coupling and reflectivity measurement, similar to the approach used by Wood [37], were employed. Note that a periodic array of cylindrical rods placed on the 2D holey structure is utilized to enhance the diffractive coupling of the incident waves to the surface modes which would otherwise be very weak. Apart from [33], other experimental contributions [38–40] unambiguously verified the existence of spoof SPPs on 2D and 1D corrugated metal surfaces and provided several useful experimental techniques for excitation and characterization of this new kind of surface mode.

Subsequently, the 1D array of grooves shown in Fig. 1(c) was developed, and the corresponding dispersion relation can be analytically given by [29]

$$k_{||} = k_0 \sqrt{1 + \frac{a^2}{d^2} \tan^2(k_0 h)}, \tag{3}$$

where a, h, and d are the width, depth, and periodicity of the groove array, respectively. The grooved metal surface can be effectively regarded as a single homogeneous layer of anisotropic material with

thickness h placed on top of a PEC surface, as depicted in Fig. 1(c). Under the condition of $k_{||}a \ll 1$, the homogeneous layer can be described as an anisotropic material with the following parameters [30]

$$[\overline{\overline{\varepsilon}}] = \begin{bmatrix} \frac{d}{a} & 0 & 0 \\ 0 & \infty & 0 \\ 0 & 0 & \infty \end{bmatrix}, \quad [\overline{\overline{\mu}}] = \begin{bmatrix} 1 & 0 & 0 \\ 0 & \frac{a}{d} & 0 \\ 0 & 0 & \frac{a}{d} \end{bmatrix}. \tag{4}$$

It should be noted that only the fundamental mode in holes or grooves is considered. Although this approximation leads to some questions on the validity of the metamaterial model [34], this effective medium description is illustrating, as it serves as a guide to design and implement the manipulation strategies of controlling surface waves on corrugated metal surfaces following SPP-like methods.

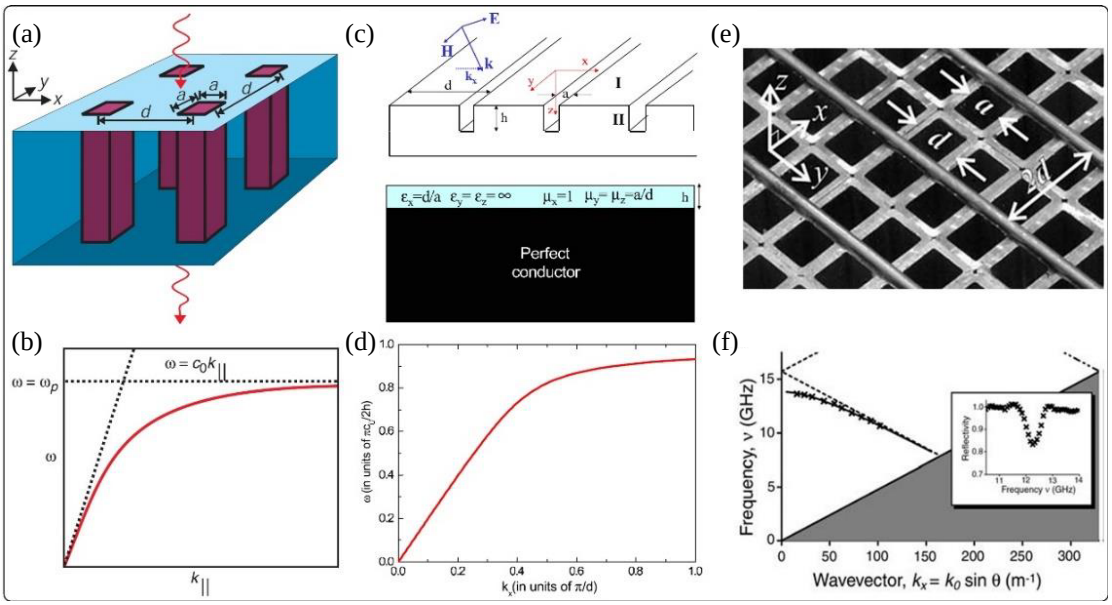

Figure 1. Spoof SPPs on subwavelength periodic metal surfaces. (a) Schematic diagram of a 2D array of holes, and (b) the corresponding dispersion curve [29]. (c) Schematic diagram of a 1D array of grooves, and (d) the corresponding dispersion curve [30]. (e) Experimental verification of the spoof SPPs with a 2D array of holes in the microwave region, and (f) the corresponding measured dispersion curve [33].

2.1.2. From Bulky to Ultrathin Structure

After the theoretical prediction [29] and experimental demonstration of spoof SPPs on both 2D and 1D corrugated metal surfaces, a variety of spoof SPP functional devices with different corrugated configurations have been developed with subwavelength field confinement at microwave and THz regimes thanks to their special propagation properties including confining, focusing, and slowing light in a subwavelength region beyond the diffraction limit. Fig. 2 illustrates various corrugated metal surfaces supporting the propagation of spoof SPPs, including 2D periodic square or round holes [33–36, 41], "mushroom" structure array [42], and 1D corrugated grooves or metal pillars [43–45], as shown in Figs. 2(a)–2(c). Specifically, in 2006, Maier et al. reported a periodically corrugated cylindrical metallic wire that can support spoof SPP waves [46, 47], as shown in Fig. 2(d). Then in Figs. 2(e) and 2(f), the theoretical and experimental verifications were implemented to illustrate the confined THz SPPs on helically grooved metal wires [48–50]. Such helically grooved metal wires can support spoof SPPs with azimuthal symmetry [49]. From the dispersion and corresponding angular properties of this chiral surface mode, it is shown that chiral spoof SPPs exhibit nonzero orbital angular momentum on the

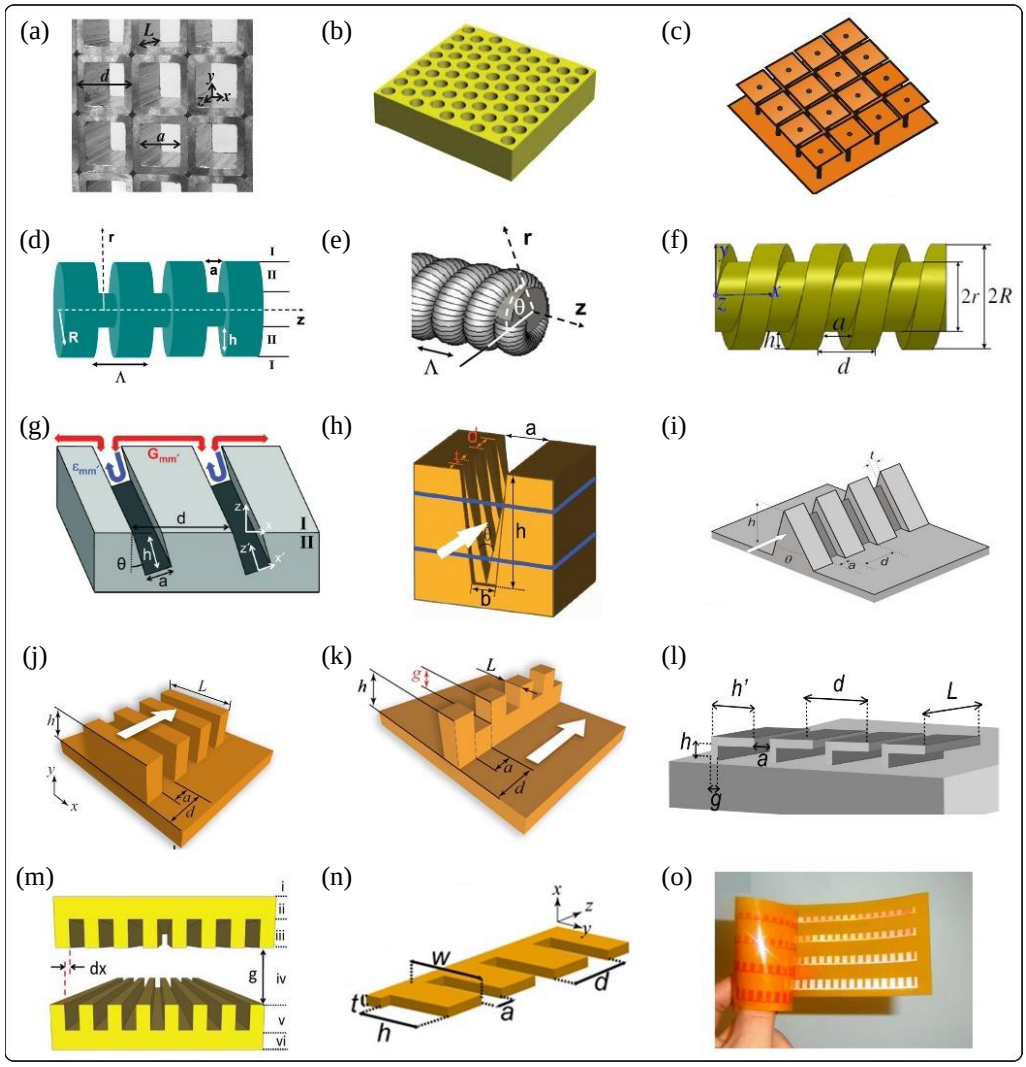

Figure 2. (a) 2D periodic square holes [33]. (b) 2D periodic round holes [41]. (c) 2D periodic "mushroom" structure array [42]. (d) Corrugated cylindrical metallic wire [46]. (e), (f) Helically grooved metallic wire [48, 50]. (g) 1D periodic array of slanted grooves [51]. (h) Channel plasmon waveguide [52]. (i) Wedge plasmon waveguide [57]. (j), (k), (l) Domino plasmon waveguide [61–64]. (m) Spoof-insulator-spoof waveguide [66]. (n), (o) Conformal plasmon waveguide [69].

helically grooved metallic wire. Interestingly, the integer or fractional orbital angular momentum can be realized by adjusting the wave vector of the surface mode. The aforementioned cylindrical and chiral spoof SPPs exhibit promising applications in energy trapping and super-focusing [50] for high-resolution THz imaging.

With the development of modern science and large-scale integration technology, the requirements for the development of integration, miniaturization, and planarization of plasmonic devices and components are becoming more and more extensive. Therefore, it is highly desired that spoof plasmonic waveguides can be optimized to a planar configuration while maintaining subwavelength field confinement and low propagation loss. Wood et al. reported that a flat PEC surface with a 1D periodic array of slanted grooves [51] can act as a 1D surface plasmonic waveguide, as shown in Fig. 2(g). To further improve the field confinement and reduce bending loss of spoof SPPs, flat metal surfaces with corrugated V-shaped grooves [52] were designed to mimic the channel plasmon polaritons in the visible light regime [53], as shown in Fig. 2(h), so that the concept of geometry-induced SPPs [29] is proposed to guide spoof channel

plasmon polaritons at THz regimes. Subsequently, some optimizations by structuring the groove walls with alternating U-shaped grooves and V-shaped grooves were proposed at both microwave [54, 55] and telecom wavelengths [56] with superior subwavelength field confinement, ultra-low bending loss, and compatibility with planar technology.

As shown in Fig. 2(i), a complementary structure with V-shaped grooves was studied by corrugating metallic wedges [57–59] resembling the properties of wedge plasmon polaritons in telecom and optical regions [60]. Subsequently, a periodic array of metallic blocks and variants standing on a metal surface, as shown from Figs. 2(j) to 2(l), was reported to support guided surface modes, namely domino plasmons [61]. Contrary to the corrugated metallic wires [45, 46] and structured grooves [48, 54, 55] or wedges [57–59], its planar geometry is more helpful in making domino plasmonic waveguides for the construction of various planar functional devices such as waveguide bends, ring resonators, tapers, power splitters, and directional couplers [62–64]. These works not only illustrate the flexibility of domino plasmons but also predict the prospects of high integration density circuits at THz frequencies. Apart from the aforementioned spoof SPP waveguides on a single structured metal surface, a spoof-insulator-spoof plasmonic waveguide [65–67], analog to a metal-insulator-metal waveguide [68], has been reported as shown in Fig. 2(m). It is revealed that the coupling between these metallic parallel plates results in the bonding and antibonding modes, and the lateral shift between two corrugated metal surfaces offer a new route to realize propagation surface modes with negative group velocity at deep-subwavelength scale thanks to the strong couplings between the bonding and antibonding surface modes.

For the production of advanced plasmonic functional devices, it is of great importance to confine the surface EM waves at a subwavelength scale and to propagate on flexible and curved surfaces. Because flexible and stretchable structures can be wrapped on curved surfaces and objects, they have advantages over devices integrated on traditional rigid wafer-based substrates in terms of wearable devices and systems. However, all of the above-mentioned spoof plasmonic metamaterials have a major limitation associated with their inherent 3D geometry. To overcome this, an important concept of conformal surface plasmons (CSPs) was proposed in 2013 by Shen et al. [69], referring to SPPs propagating on flexible and ultrathin paper-like dielectric films that can be folded, bent, and even twisted to control CSPs with long propagation distances in broadband at low frequencies, as shown in Figs. 2(n) and 2(o). In this design, the CSP waveguide is essentially a periodic groove corrugated on a metal film with nearly zero thickness [70]. It is revealed that when the thickness gradually decreases from infinity, the dispersion curve deviates further away from the light line accordingly. On the other hand, when the thickness is less than $0.02d$ (d is the period of the unit cell), the dispersion curve remains almost unchanged. In other words, when the thickness is decreased to be finite, the two ports of each cavity in the $\pm x$ directions are open, and therefore, the magnetic field is unconstrained. This is why the SPP waves can be supported on a thin metal film with nearly zero thickness. Additionally, considering that the metal layer in the current printed circuit board (PCB) technology is usually on the order of 1 μm, spoof SPP waveguides can be fabricated with low cost and high reliability at microwave frequencies.

2.1.3. Efficient and Broadband Excitation

The concept of plasmonic metamaterials has proven to be very useful in the production of highly confined surface EM waves at low frequencies. Generally, plasmonic metamaterials consist of metal surfaces decorated with 1D arrays of subwavelength grooves/gratings, 2D arrays of subwavelength holes/dimples, or 3D metal wires (a periodic array of radial grooves is drilled). The conversion from spatial propagating waves to SPPs has been well studied using prisms [33–36], gratings [71, 72], and dipole or monopole antennas [69–71, 73–76]. However, due to the mismatch of momentum between these two different modes, the conversion efficiency is relatively low, which limits its real applications. To address this mismatching issue, a gradient-index metasurface has been proposed to transform spatial propagating waves to SPPs efficiently [77]. In practice, most advanced microwave and THz plasmonic functional components and devices need to be connected to the conventional microwave or THz circuits, which are mainly composed of two-conductor transmission lines (such as microstrip lines or coplanar waveguides, CPWs) and relevant devices. In this section, we will review various matching schemes that have been proposed to efficiently excite spoof SPPs in broadband.

As shown in Fig. 3(a), an efficient mode conversion scheme was first proposed by Ma et al. to convert the traditional guided TEM wave in a coplanar waveguide (CPW) to the SPP wave in a metallic

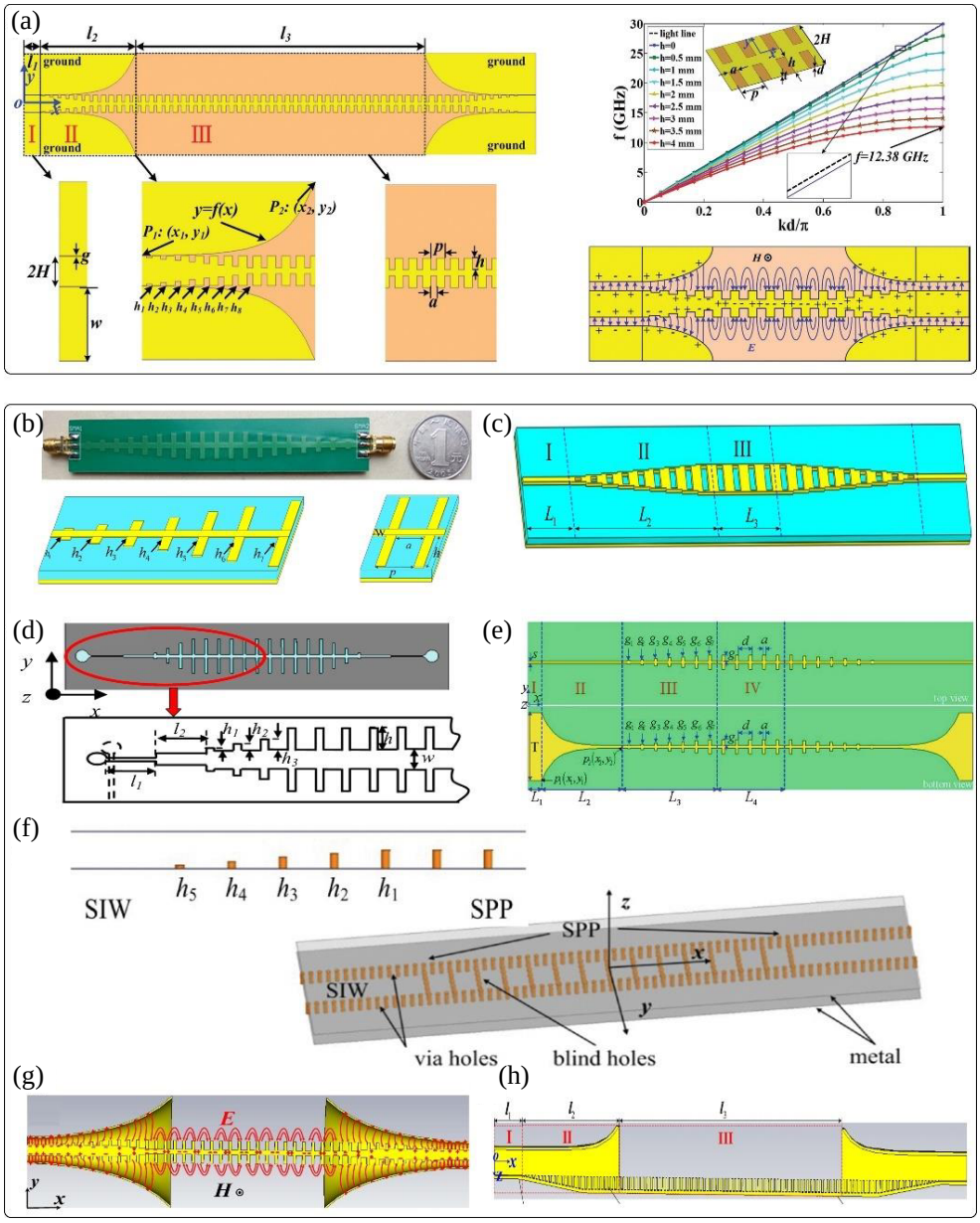

Figure 3. Broadband and high-efficiency excitation of spoof SPPs, (a) by a CPW [78], (b), (c) by a microstrip line [79, 80], (d) by a slot line [81], (e) by a two-strip transmission line [82], (f) by a SIW [110], (g) by a coaxial waveguide [107], (c) by a rectangular waveguide [108].

strip consisting of double-side corrugated grooves [78]. Considering the large mismatch of wavenumber between the guided wave supported by CPW in Region I and the SPP supported by corrugated metallic strip in Region III, a smooth bridge structure is designed in Region II. This bridge has a Goubau ground to realize impedance matching and gradient grooves with gradient depth to realize the momentum matching, as shown in the upper right corner inset of Fig. 3(a). In this manner, excellent transmission efficiency from CPW to SPP transmission line and then back to CPW is achieved in broadband. In the experiment, a transmission coefficient of higher than -0.6 dB from 6 to 12 GHz is obtained. Borrowing such an idea, many other conversion schemes have also been proposed for efficient bridging SPP transmission lines and different types of traditional waveguides. Fig. 3(b) shows a broadband and high-efficiency excitation of SPP waves by a microstrip line [79]. In this design, a gradient corrugated

metallic strip is applied to realize a gradual change of the wave vector from the microstrip to the SPP transmission line. Fig. 3(c) shows another efficient excitation of SPP waves supported by a metal strip with gradient periodic holes through a grounded microstrip line [80]. Here, it should be noted that the corrugated metallic strip with the ground also possesses SPP-like dispersion characteristics and a highly localized surface EM field. As shown in Fig. 3(d), an important efficient excitation of odd SPP mode supported in a face-to-face corrugated metal strip is realized by a traditional slot line [81]. This corrugated metal strip is also regarded as a spoof-insulator-spoof plasmonic waveguide. Fig. 3(e) describes a double-layer CSP waveguide converting scheme [82], where a microstrip line is bridged to a dual-strip SPP transmission line constructed by mirror arranged unit cells. It is seen that SPP transmission lines with dual conductors are easier to couple with traditional transmission lines because their electric fields have perpendicular components.

Since CSP waveguides and efficient bridge structures can be fabricated with the standard PCB technology, it is easy to integrate them with conventional transmission lines. Then various efficient functional devices were proposed, such as broadband and high-efficiency mode converter [83], frequency splitter/combiner [84, 85], plasmonic filter [86–88], slow-wave transmission line [89, 90], crosstalk suppression [91–95], wavelength demultiplexer [96–98], as well as various spoof SPP based antennas [99–106].

On the other hand, in Figs. 3(f)–3(h), traditional coaxial waveguide [107], rectangular waveguide [108, 109], and substrate integrated waveguide (SIW) [110–112] were employed for efficient excitation of the spatial 3D spoof SPPs, in which a metal cylindrical wire corrugated with subwavelength gradient radial grooves [107], a slab waveguide pasted with stacked gradient domino metal blocks [108], and a row of metal vias with gradual depth [110] were introduced and designed for realizing a smooth bridge between these traditional 3D cavity waveguides and spoof SPP waveguides. The experimental results verified the efficiency of these schemes.

To summarize, compared with conventional microwave waveguides, spoof SPP waveguides show some unique features from the engineering point of view. For example, the SPP waveguide supports the confined surface mode in a wide frequency band with an asymptotic frequency, while most conventional double-conductor transmission lines support the quasi-TEM mode without a cut-off frequency. The enhanced field confinement is the most important and unique property of spoof SPP, leading to exotic features that cannot be found in traditional microwave waveguides, e.g., significantly low crosstalk [91–95], low propagation loss, and low radiation loss at bending areas [84]. Because most energy of spoof SPPs is confined at a subwavelength scale, only a limited portion radiates into the free space. Additionally, efficient and broadband excitation of such surface mode makes it a solid step on the road to widespread applications and provides a constructive pathway for its potential applications in future wireless communications, large-scale integrated circuits, and many other fields.

2.1.4. Active Nonlinear SPP Devices and Circuits

A very active area of plasmonic research is the design of spoof SPP-based integrated devices and circuit systems. This was originally motivated by the development of CSPs supported in ultrathin metal films, providing a natural platform for the design of integrated functional devices due to their planar structure. As we all know, the transmission line and semiconductor technology have laid the foundation for modern electronic information technology. Active circuit system in microwave engineering generally takes advantage of the semiconductor-based components and chips available at those frequency ranges. Actually, active devices, such as oscillators, analog switches, frequency mixers, multiplier/dividers, and amplifiers play a vital role in the function and performance of the circuit system. Taking these into account, active SPP-based components and circuit design are of great importance for real applications.

A significant property of the spoof SPP waveguide is its tunability of the dispersion by adjusting the geometries, providing extended flexibility compared to traditional microwave devices. In the active circuits, such dispersion tunability can be further enhanced with active control by loading active elements, such as varactor and active chip, to achieve nonlinear tuning of spoof SPPs, offering dynamic and programmable control of the signals for different requirements. Moreover, some nonlinear effects, such as second harmonics generation, can be significantly enhanced thanks to the strong confinement of surface EM waves and enhanced field intensity features of spoof SPPs.

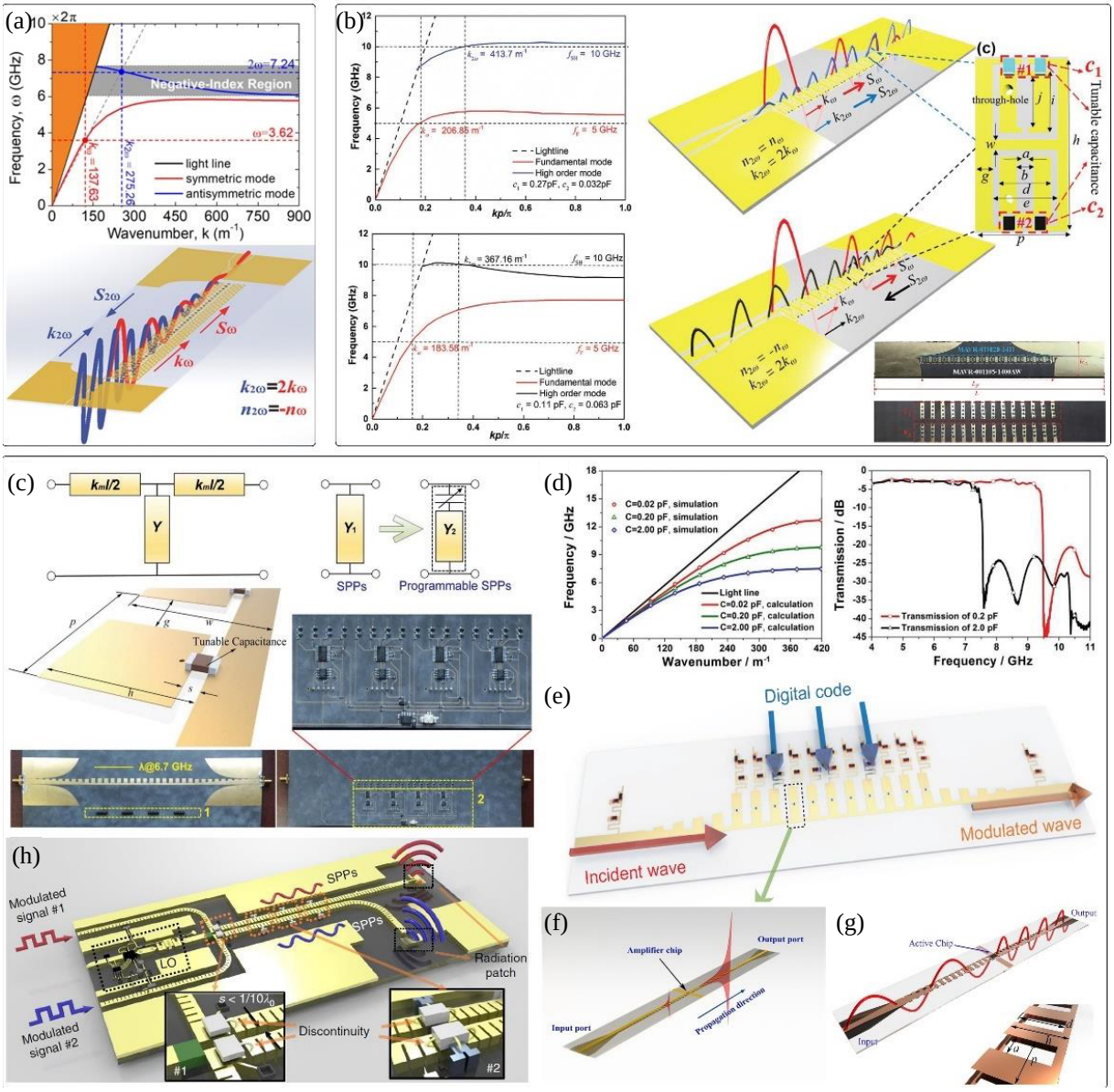

Figure 4. (a), (b) Backward and forward phase-matched SHG [113, 114]. (c), (d), (e) coding, programmable and modulation of digital spoof SPPs [115–117]. (f) Active amplification of spoof SPPs [118]. (c) SHG of nonlinear SPPs with active chip [121]. (d) Spoof SPPs based communication system [124].

An important work for active SPP circuits is the realization of a backward phase-matching for second harmonic generation (SHG) of spoof SPP waves at microwave frequencies, where the nonlinear properties are generated from the varactors loaded on a specifically designed ultrathin CSP waveguide [113], as shown in Fig. 4(a). In such a nonlinear CSP waveguide, the backward phase-matching conditions of $k_{2\omega} = 2k_\omega$ and $n_{2\omega} = -n_\omega$ are satisfied simultaneously, where k_ω and $k_{2\omega}$ are the wave numbers, and n_ω and $n_{2\omega}$ are the refractive indexes of the fundamental and second-harmonic waves, respectively. Compared with the alternative methodology in optical bands, the conversion efficiency of the backward phase-matching for SHG in such an active CSP waveguide is increased by $5 \sim 6$ orders of magnitude. Subsequently, reconfigurable SHGs [114] were proposed on such nonlinear SPP waveguide by changing the capacitances of the varactors loaded on the SPP unit structure, to dynamically switch the forward phase-matching conditions ($k_{2\omega} = 2k_\omega$, $n_{2\omega} = n_\omega$) and backward phase-

matching conditions, as shown in Fig. 4(b). As a result, the forward and backward phase-matching SHGs have been experimentally demonstrated in the same frequency of 5 GHz for the fundamental mode and 10 GHz for the second harmonic mode with high conversion efficiency.

Apart from the varactor, the spoof SPP waveguide loaded with other active components, such as positive-intrinsic-negative (PIN) junction diode and Schottky diode, can be used to realize coding and programmable control of spoof SPPs [115–117]. Different from the continuous control of dispersion relation based on varactors, PIN and Schottky diodes have two discrete states as on- and off-states. PIN diode can also be positioned between the spoof SPP unit cell and the parallel branch so that such an active spoof SPP waveguide can be switched between two discrete dispersion states in the on-state (namely code 1) and off-state (namely code 0), as shown in Figs. 4(c)–4(e).

In communication systems, a power amplifier is a critical component to compensate for the path loss. However, traditional RF/microwave amplifiers that rely on nonlinear amplifier chips may suffer from gain and phase distortions. To overcome this, a spoof SPP-based amplifier [118] has been designed, as shown in Figs. 4(f) and 4(g). The SPP mode is supported by a waveguide formed of two ultrathin comb-shaped metal strips placed on top of each other in an antisymmetric manner. A commercially available low-loss power amplifier chip is employed to amplify the spoof SPPs traveling through the waveguide, where two microstrip lines as input and output ports are designed to provide a compact mode transition. As a result, spoof SPP waves are efficiently amplified in the range of 6 to 20 GHz with a gain of more than 20 dB. Subsequently, a parametric amplifier in an ultrathin reconfigurable SPP waveguide has been proposed [119]. The measured parametric gain can reach up to 9.14 dB within six wavelengths. By changing the bias voltage of varactors, the multi-frequency parametric amplification of spoof SPP signals was realized as well.

Generally, spoof SPP transmission lines can provide the demanded harmonic suppression without an extra filtering module. This is a significant and distinctive advantage over traditional transmission lines. The above strategy of loading active components or chips in a subwavelength scale on the spoof SPP transmission lines have been directly extended to realize other active spoof SPP devices, such as switches [120], amplifiers [118], second harmonic generators [113, 114, 121], Wilkinson power dividers [122], and multi-scheme digital modulators [123]. On account of the exotic features of spoof SPP transmission lines and the passive and active components with high performance and reconfigurable functionalities, integrated spoof SPP circuits and systems for wireless communication applications were realized [124], as shown in Fig. 4(h).

2.1.5. MGs-Induced Spoof LSPs

Generally, there are two manifestations of surface plasmons. One is the SPPs that propagate on the metal surface, while the other is the localized surface plasmons (LSPs) that are confined on a closed surface or particle [125]. In optics, LSPs have been widely used in surface-enhanced Raman spectroscopy [126], photovoltaics [127], and nonlinear enhancement due to their advantage of localized field enhancement in a subwavelength region. It has been shown that a periodically textured 2D PEC cylinder can sustain surface EM modes similar to optical LSPs, called spoof LSPs [128], which provide a route to inherit almost all the characteristics of optical LSPs to the lower frequencies. Spoof LSPs can enhance light-matter interaction at low frequencies by inheriting the subwavelength confinement feature of optical LSPs. Moreover, its EM properties are dominantly controlled by the geometry of corrugations, providing great flexibility in engineering the EM behaviors in corrugated structures with closed surfaces. More importantly, the Ohmic loss, a well-known bottleneck in optical surface plasmonics, can be ignored for spoof LSPs due to the perfect conductor characteristics of most noble metals at lower frequencies. Hereinafter, we will review the MGs-induced spoof LSPs focusing mainly on its basic physical concept, theory, design method, experimental realization, and advancement.

As shown in Fig. 5(a), Pors et al. [128] illustrated a simple 2D metallic disk with corrugated grooves along its azimuthal direction that can support low-frequency spoof LSPs. In this design, the metallic disk was corrugated with N grooves. A dielectric material with a refractive index of n_g is filled in the grooves, and the surrounding medium is assumed to be free space. The outer radius R and grooves number N are set to meet the condition $a,\ d \ll \lambda_0$, where $d = 2\pi R/N$, and λ_0 is the operation wavelength in free space (the same below). Thus, the asymptote frequency $\omega_a = \pi c/(2hn_g)$ corresponding to the spoof SPPs with similar grooves can also be determined by the groove depth h

and refractive index n_g. The resonance condition for each spoof LSP mode can be determined by the following transcendental equation [128]

$$S_n^2 \frac{H_n^{(1)}(k_0 R)\, f}{H_n^{(1)'}(k_0 R)\, g} = n_g, \tag{5}$$

where $f = J_1(k_0 n_g r)\ Y_1(k_0 n_g R) - J_1(k_0 n_g R) Y_1(k_0 n_g r)$ and $g = J_0(k_0 n_g R) Y_1(k_0 n_g r) - J_1(k_0 n_g r) Y_1(k_0 n_g R)$ with J_0 and J_1 (Y_0 and Y_1) being the first kind of zero-order and first-order Bessel functions, respectively; n is the mode number; and $S_n = \sqrt{a/d}\sin c[na/(2R)]$. The '' means differentiation with respect to the argument in parenthesis. It is worth noting that all details about the unit cell are found in S_n, which, for subwavelength texturing ($a \ll R$), approximates to $S_n \cong \sqrt{a/d}$.

The physical properties of spoof LSPs can be shown by comparing them with a metallic particle carrying Drude permittivity $\varepsilon(\omega) = 1 - \omega_p^2/\omega^2$, where ω_p is the plasma frequency of the metal. The spoof LSP particle has nearly the same scattering cross-section (SCS) as a Drude-type metallic particle, where $\omega_a = \omega_p/\sqrt{2}$. To characterize the similarity of its EM characteristics with its optical counterpart, an effective metamaterial description was first introduced. This model can be regarded as a core-shell structure (PEC core and metamaterial shell). The relative permittivity and relative permeability tensors of the effective metamaterial in the cylindrical coordinate can be equivalence to [128]

$$\varepsilon_\varphi = n_g^2 d/a, \quad \varepsilon_\rho = -\infty, \quad \varepsilon_z = -\infty, \tag{6a}$$

$$\mu_\varphi = a/d, \quad \mu_\rho = 1, \quad \mu_z = a/d. \tag{6b}$$

This metamaterial approximation also has the advantage of an analytical treatment due to the simple geometry. With the above metamaterial approximation, it is straightforward to obtain the analytic expression for the SCS as [128]

$$\sigma_{scs} = \frac{4c_0}{\omega} \sum\nolimits_{n=-\infty}^{\infty} |C_n|^2, \tag{7a}$$

where

$$C_n = -i^n \frac{\frac{a}{d} J_n(k_0 R)\, f - n_g J_n'(k_0 R)\, g}{\frac{a}{d} H_n^{(1)}(k_0 R)\, f - n_g H_n^{(1)'}(k_0 R)\, g}. \tag{7b}$$

It is evident from Equation (7b) that the resonance condition (zero in the denominator) is identical to Equation (5) just with $S_n = \sqrt{a/d}$.

The first experimental demonstration was conducted by Shen and Cui at microwave frequencies [129]. In the experiment, a corrugated copper disk with a thickness of 0.018 mm (outer radius $R = 10.0$ mm, inner radius $r = 0.25R$, groove width $a = 0.4d$, and groove number $N = 60$) is printed on a 0.4 mm-thick polyimide substrate by the standard PCB technology, as shown in the inset on the far right of Fig. 5(a). The spoof LSP modes were characterized by the near-field excitation and detection methods. Various multipolar modes were observed directly on the corrugated copper disk, including electric-dipole, -quadrupole, -hexapole, -octopole, -decapole, -dodecapole, and -quattuordecpole modes, as shown on the right side of Fig. 5(a). It should be noted that there are resonances shift when the thickness of the particle is reduced from an infinitely long textured cylinder [128] to a corrugated disk of finite thickness [129]. While this is the expected behavior from particle plasmonics, the quasi-degeneracy between the electric and magnetic modes is lifted. Specifically, the electric and magnetic LSPs split in such a way that the latter shifts to higher frequencies than the former. In general, while infinitely long cylinders with periodic subwavelength corrugations present a magnetic LSP that is very close in frequencies to the electric LSP, finite long corrugated disks support a magnetic LSP at a different frequency from the electric LSP. As opposed to the corrugated PEC disk, a hollow textured PEC cylinder has been demonstrated to support magnetic LSP at a lower frequency than the electric LSP [130], as shown in Fig. 5(b).

Another important approach to realize magnetic LSP mode is to use spiral metallic grooves which can increase the groove depth h with a constant radius R. An appropriate choice of the spirals' length allows the spectral shift of spoof LSPs to wavelengths much larger than the particle size, giving rise to strong EM field localization on its surface. This property also adds additional degrees of freedom

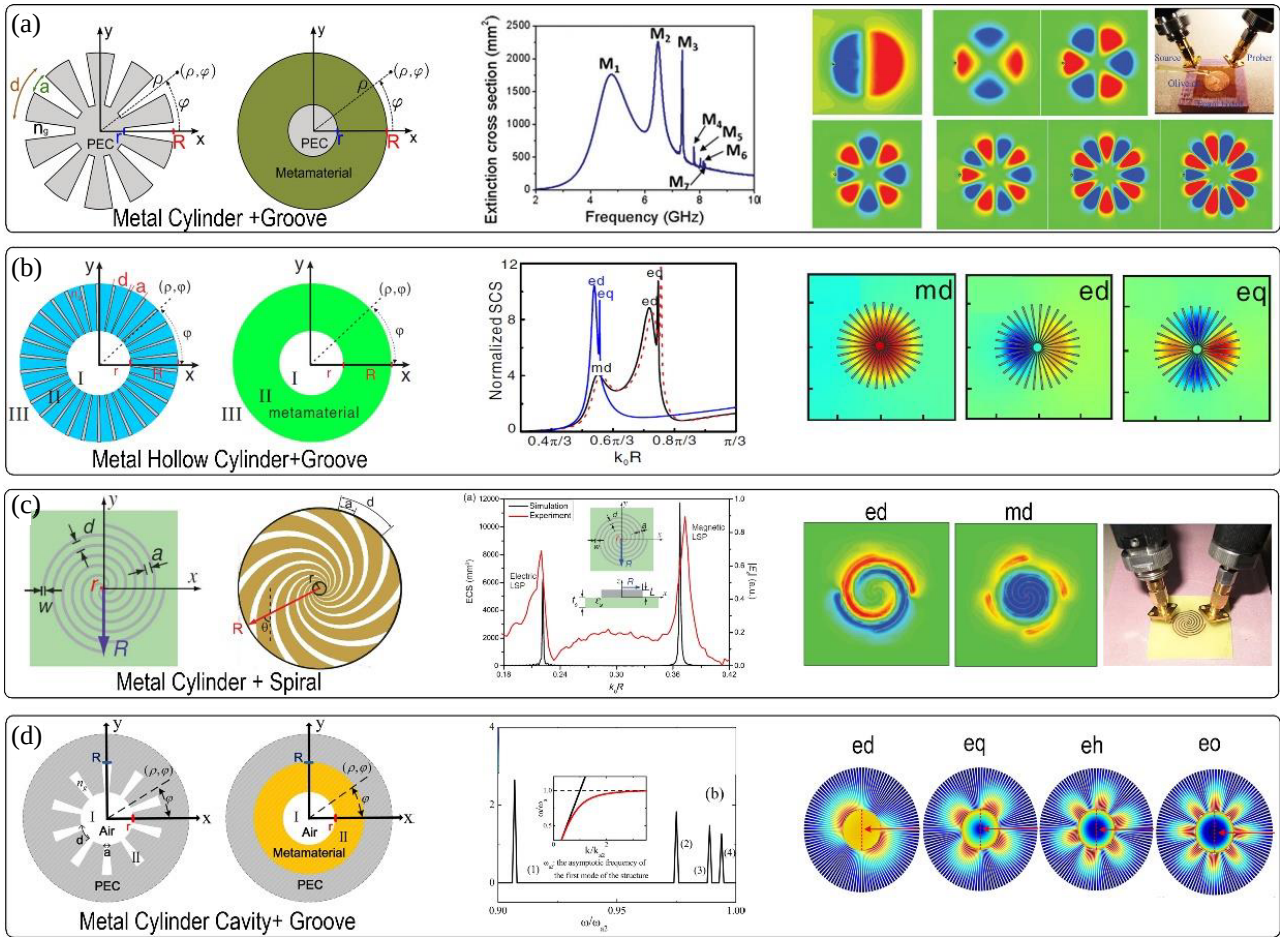

Figure 5. Spoof LSP supported in, (a) a structured PEC cylinder [128], (b) a hollow textured PEC cylinder [130], (c) a periodic spiral metal strip [131, 132], (d) a periodically textured closed cylinder cavity [133].

for the design of spoof plasmon structures, greatly increasing the tunability of these devices. The first proposal is illustrated in Fig. 5(c), which was implemented in the experiment [131] by depositing a 0.018 mm thick copper disk that is textured with spiral grooves on a 0.8 mm thick FR4 substrate with relative permittivity of 3.5. Experimental results show that the structure is close to 1/10 of the wavelength in the vacuum at the dipole resonance, whose field pattern is illustrated on the right of Fig. 5(c). To further understand the origin of the deep-subwavelength property and magnetic LSP mode, Liao et al. [132] developed an effective medium model to describe the spiral geometry, where a logarithmic spiral characterized by a spiral angle θ is used and parameterized as $x(t) = re^{t/\cot\theta}\cos(t)$, $y(t) = re^{t/\cot\theta}\sin(t)$. With the metamaterial approximation, the effective permittivity and permeability can be written in cylindrical coordinates as [132]

$$\varepsilon^{-1} = \frac{a}{2dn_g^2}\begin{bmatrix} 1-\cos 2\theta & -\sin 2\theta \\ -\sin 2\theta & 1+\cos 2\theta \end{bmatrix}, \quad \mu^{-1} = \frac{d}{a}, \tag{8}$$

where the permittivity tensor is restricted in the xy-plane. By introducing the above permittivity and permeability tensors into the Mie theory, the resonance condition characterized by the azimuthal

angular momentum n can be written as [132]

$$\frac{2a\cos\theta}{d}\sin c^2\left(\frac{na}{2R}\right)\frac{H_n^{(1)}(k_0R)}{H_{n-1}^{(1)}(k_0R)-H_{n+1}^{(1)}(k_0R)}=\frac{n_gq}{p}, \tag{9}$$

where $p = J_1(k_0n_gr/\cos\theta)\,Y_1(k_0n_gR/\cos\theta) - J_1(k_0n_gR/\cos\theta)\,Y_1(k_0n_gr/\cos\theta)$ and $q = J_0(k_0n_gR/\cos\theta)\,Y_1(k_0n_gr/\cos\theta) - J_1(k_0n_gr/\cos\theta)\,Y_1(k_0n_gR/\cos\theta)$. This model allows for a comprehensive understanding of the electric and magnetic LSP resonances (both fundamental and higher-order modes) supported by the spiral structure. Experimental results show that a larger spiral angle θ can render a larger resonance wavelength while keeping the outer radius R, inner radius r, and refraction index n_g unchanged.

The aforementioned MGs-induced LSPs show that field confinement and enhancement are all in an open space. Actually, the spoof LSP resonances can also exist in a complementary structure, a periodically textured closed cavity [133], which has been demonstrated to show different field confinement features compared with the above MGs-induced LSPs in open space. In Fig. 5(d), a textured PEC circular cavity with radius R is overlaid with the subwavelength inward radial groove of height $h = R-r$ and periodicity $d = 2\pi r/N$, and the medium in the inner cylinder with radius r is assumed to be air. It was remarked that TM modes are concentrated in the inner air region and are not plasmon-like modes. With good approximation that diffraction can be ignored when $d \ll \lambda_0$, the resonance condition for such individual modes has been derived by Li et al. as the following transcendental equation [133]

$$\mathrm{Sinc}^2\left(\frac{ma}{2r}\right)\frac{aJ_m(k_0R)\,f}{dJ'_m(k_0R)\,g}=n_g, \tag{10}$$

where $f = Y_1(k_0n_gr)\;J_1(k_0n_gR) - Y_1(k_0n_gR)J_1(k_0n_gr)$ and $g = Y_1(k_0n_gR)J_0(k_0n_gr) - Y_0(k_0n_gr)J_1(k_0n_gR)$; m represents the wavelength number in the circumferential φ direction; and n corresponds to the half wavelengths number in the radial ρ direction. Li et al. find that there are infinite spoof LSPs modes with their resonance frequencies approaching the asymptote frequency when m increases for a certain n in such textured cavity. Obviously, the resonances distribution of these spoof LSP modes shown on the right side of Fig. 5(d) is quite different from that of the TE modes in a conventional circular cavity. Moreover, the resonance frequency of each TE_{mn} mode can be tuned freely by adjusting the groove depth, the refractive index n_g of the medium inside the cavity. These spoof LSPs resemble the natural LSPs occurring in closed Drude metal cavities in the optical regimes, which can be an important candidate in the design of ultrahigh-Q plasmonic resonant components and devices at microwave and THz frequencies.

It should be pointed out that apart from the above tuning method, many other degrees of freedom for controlling spoof LSPs can also be utilized. A periodically textured closed surface with multiple groove depths in one periodicity can support multi-band spoof LSPs [134, 135], where band spoof LSPs resemble those generated by a single periodically textured closed surface with the corresponding groove depth. Subsequent different designs have shown the versatility of particles corrugated with grooves of parallel walls, and many different geometries have been studied, including corrugated ring structures [136, 137], open particles [138], and defect-trapped structures [139]. Enhanced high-order resonances [140], Fano resonances with two coupled LSP particles [141, 142], frequency selective propagation in particle chains [143], the invisibility of near-field energy transport [144], and THz Purcell effect enhancement [145] have also been demonstrated. Additionally, gradient-depth grooves and gradient-length spirals have been designed for achieving broadband harvesting of EM energy [146, 147]. On the other hand, the magnetic LSP modes supported by ultrathin spiral particles have also been extensively studied. High-order magnetic LSPs were demonstrated in [148], and the modes supported by the complementary structure were also studied [149, 150]. The magnetic coupling among stacked spiral particles was studied in [151]. Spoof plasmon hybridization [152] between two closely spaced magnetic LSP particles yields new hybrid modes not found in individual constituents, allowing for the engineering of resonance properties and field enhancement capabilities. The EM interference between the electrical and magnetic LSPs in unidirectional super-scattering has been reported in [153, 154]. Moreover, spoof LSPs have also been employed to design ultra-compact integrated photonic circuits in microwave frequencies [42, 85, 155], where the spoof-LSPs sustained by ultrathin structures were coupled to the propagation CSP. All these works demonstrate the potential of spoof LSPs for applications in ultra-compact integrated photonic circuits in the microwave and THz spectrum.

3. SPOOF SURFACE PLASMONS ARISING IN SUBWAVELENGTH HIGH-INDEX CONTRAST GRATING

The characteristics of field confinement on the surface of metals and the intrinsic ohmic losses of most real metals still result in a non-negligible propagation loss of the spoof SPPs in long-range transmissions, especially at the upper end of microwave and THz frequencies. To increase the propagation length while retaining the subwavelength confinement and enhancement feature of spoof SPPs, it is of great importance to reduce the metallic losses. In this respect, Li et al. proposed a new concept of high-contrast gratings (HCGs)-induced SPPs [156], which is supported on the surface of corrugated HCGs on a PEC plane, as shown in Fig. 6(a). Here, we will review the HCGs-induced SPPs and LSPs from several aspects such as fundamental EM behaviors, numerical simulation, and experimental realization.

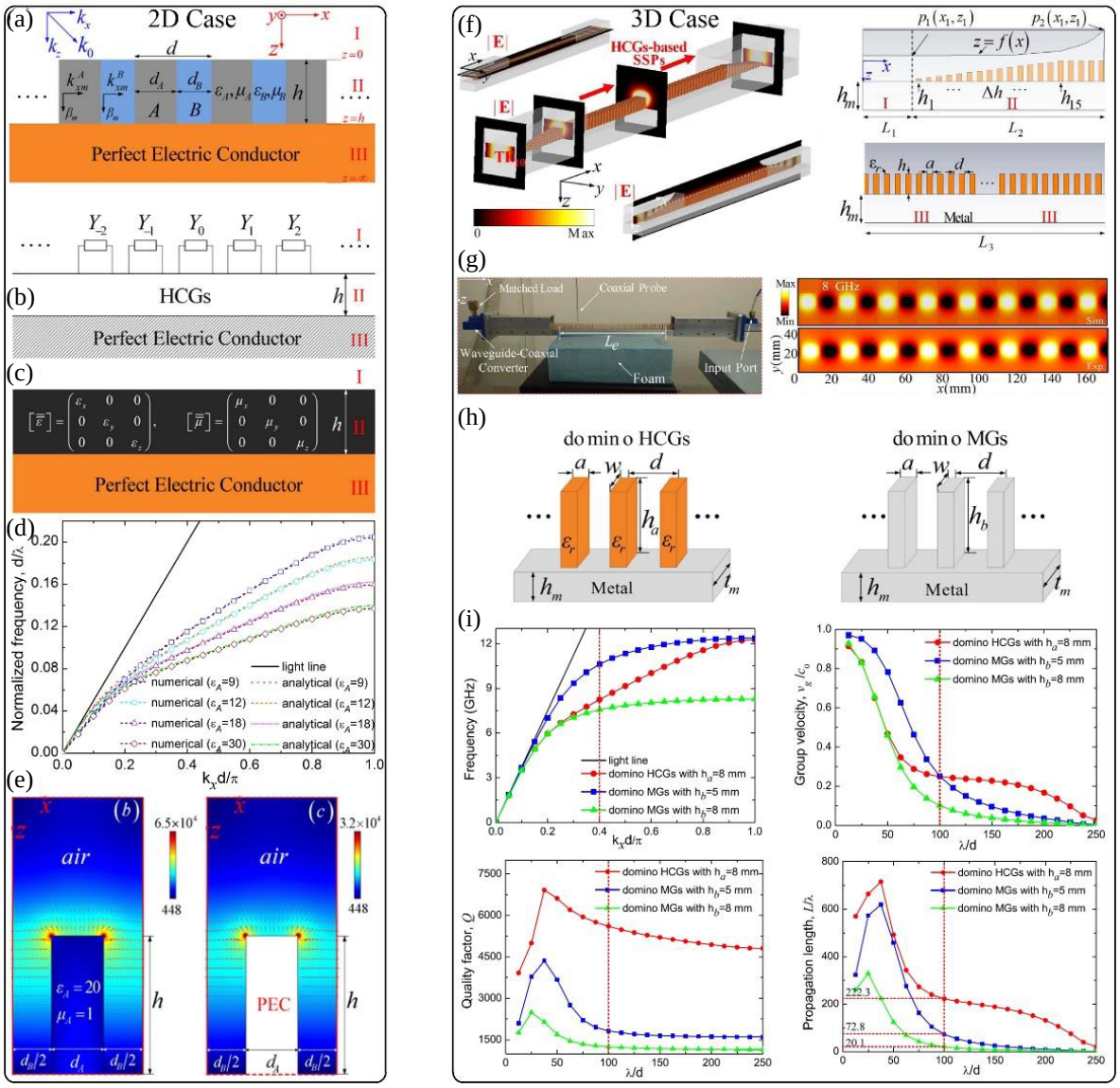

Figure 6. (a), (b), (c) 2D HCGs structure [156] and its corresponding equivalent multimode network and effective medium approximation. (d) Dispersion curves of the 2D HCGs-induced SPPs [158]. (e) Surface electric field distributions [156]. (f), (g) Broadband and ultralow-loss HCGs-induced SPP waveguide [158]. (h), (i) Performance comparison between the 3D HCGs- and MGds-induced SPPs [158].

3.1. HCGs-Induced SPPs

For a specific surface EM mode, the dispersion relation plays a critical role in understanding the physical mechanism behind it. An approximate dispersion equation of the HCGs-based SPPs based on a 2D subwavelength HCGs array is analytically given in [156]. As shown in Fig. 6(a), the subwavelength HCGs array is divided into three regions: Region I the air, Region III the semi-infinite PEC plate, and Region II the HCGs array consists of medium Blocks A and B with width d_A and d_B, relative permittivity ε_A and ε_B, relative permeability μ_A and μ_B, and height h. Applying the Floquet theorem, when a TM-polarized plane wave incidents upon the surface of the structure, the relevant EM eigenmodes in Region II will produce a series of Bloch waves characterized by the transverse wave vectors $\kappa_{xm} = k_x + 2m\pi/d$ ($d = d_A + d_B$, $\lambda \gg d > d_A$, d_B) along the x-direction and perpendicular wave vectors β_m along the z-direction with $m = 0, \pm1, \pm2, \ldots$. The fields of each eigenmode also consist of an infinite set of space harmonics whose propagation factors along the x-direction meet the Floquet condition $k_{xn} = k_x + 2n\pi/d$ (k_{xn} is the wave vector of the nth space harmonic and $n = 0, \pm1, \pm2, \ldots$). Due to the spatial periodicity of the HCGs in the x-direction, the fields in Region I also contain an infinite set of space harmonics with the transverse wave vectors k_{xn} and perpendicular wave vectors $k_{zn} = \sqrt{k_0^2 - k_{xn}^2}$. To obtain the analytical dispersion relation of the HCGs-induced SPPs, a classical eigenmode issue when the HCGs region in Fig. 6(a) is regarded as an unbounded periodical array without the metal and air needs to be first addressed [157], in which the fields in the unbounded HCGs can be expressed as a superposition of the obtained characteristic Floquet functions. After applying the multimode network theory combined with the Floquet condition, where the standard matching boundary condition is employed and shown in Fig. 6(b), the dispersion relation of eigenmodes in the unbounded HCGs can be written as [156]

$$\cos(\kappa_{xm} d) = \cos\left(k_{xm}^A d_A\right)\cos\left(k_{xm}^B d_B\right) - \frac{1}{2}\left(\frac{\varepsilon_A k_{xm}^B}{\varepsilon_B k_{xm}^A} + \frac{\varepsilon_B k_{xm}^A}{\varepsilon_A k_{xm}^B}\right)\sin\left(k_{xm}^A d_A\right)\sin\left(k_{xm}^B d_B\right), \tag{11}$$

in which $k_{xm}^A = \sqrt{\mu_A \varepsilon_A k_0^2 - \beta_m^2}$ and $k_{xm}^B = \sqrt{\mu_B \varepsilon_B k_0^2 - \beta_m^2}$.

Only the fundamental surface mode ($m = 0$) is considered, and all the high-order diffraction effects are neglected when the generalized transverse resonance method is used. The dispersion relation of the 2D HCGs-induced SPPs can be rigorously derived when $k_x > k_0$ as [156]

$$\frac{\sqrt{k_x^2 - k_0^2}}{\beta_0} = \frac{d_A/\varepsilon_A + d_B/\varepsilon_B}{d_A + d_B}\tan(\beta_0 h). \tag{12}$$

Subsequently, the dispersion curves of the HCGs-induced SPPs can be calculated by combining Equations (11) and (12), as shown in Fig. 6(c), where four curves with different dielectric contrasts of $\varepsilon_A/\varepsilon_B$ are 9, 12, 18, and 30 when $\varepsilon_B = 1$, $\mu_A = \mu_B = 1$, $h = 2d$, and $d_A = 0.4d$ are demonstrated.

It is worth commenting on the coincidental form of the dispersion equations between HCGs- and MGs-induced SPPs. Equation (12) and Equation (14) in [128] exhibit the same form except that the denominator of the left-hand side term in Equation (12) is wave vector β_0, which is the dominant mode in the terminal short-circuit cavity with dielectrics on both sides. As described in [156], Equation (12) is a generalized form of spoof SPPs. Because if $\varepsilon_A \to -\infty$, Block A will become a PEC, and then both the electric and magnetic fields inside Block A will be zero, and the fundamental mode in the short-ended waveguide will be a TEM waveguide mode trapped only inside Block B with perpendicular wave vector $\beta_0 = k_0\sqrt{\varepsilon_B}$. Thus, Equation (12) will be degenerated into the form of the MGs-induced SPPs in [128]. In addition, from the perspective of surface electric field distribution in Fig. 6(d), the HCGs-induced SPPs also behave in the same manner as the MGs-induced SSPs. Different from MGs-induced SPPs, HCGs-induced SPPs can be engineered by tuning both the geometrical and medium parameters, which adds more degree of freedom to define and control their EM characteristics.

As mentioned in [156], HCG-induced SPPs can also be described with an effective medium approximation [157] if the HCGs are regarded as a single homogeneous but anisotropic medium layer of thickness h on top of the PEC surface. The corresponding relative permittivity and permeability

tensors would have the following diagonal forms

$$[\overline{\overline{\varepsilon}}] = \begin{bmatrix} \dfrac{d_A + d_B}{d_A/\varepsilon_A + d_B/\varepsilon_B} & 0 & 0 \\ 0 & \dfrac{\varepsilon_A d_A + \varepsilon_B d_B}{d_A + d_B} & 0 \\ 0 & 0 & \dfrac{\varepsilon_A d_A + \varepsilon_B d_B}{d_A + d_B} \end{bmatrix}, \quad [\overline{\overline{\mu}}] = \begin{bmatrix} 1 & 0 & 0 \\ 0 & 1 & 0 \\ 0 & 0 & 1 \end{bmatrix}. \tag{13}$$

To demonstrate the ultra-low loss and high confinement features of the HCGs-induced SPPs, a wideband plasmonic waveguide composed of a domino array with high refractive index dielectric blocks of subwavelength periodicity on an aluminum substrate was designed [158], as shown in Fig. 7(f). A smooth bridge has been introduced for efficient excitation of the HCGs-induced SPPs in a rectangular waveguide. Simulated and experimental results demonstrate that such a waveguide shows strong field localization at the interface [Fig. 7(g)] and excellent transmission performance in broadband. Comparisons between the HCGs- and MGs-induced SPPs in terms of dispersion relations, field distributions, and transmission loss show that it is possible to address the tradeoff between higher field confinement and larger propagation loss using the HCGs-induced SPPs, as shown in Fig. 7(i) [158]. More importantly, the EM characteristics of the HCGs-induced SPPs can be engineered at will by tuning both the geometrical and medium parameters. Thus, such as HCGs-induced tunable narrowband or wideband miniaturized filters, directional couplers, resonators, etc. could be further considered for practical applications. Additionally, full dielectric induced SPPs could be realized by using a dielectric substrate instead of the metal plate, and ultrathin HCGs-induced SPPs could also be realized thanks to the traditional screen printing and low-temperature co-fired ceramic techniques shortly.

3.2. HCGs-Induced LSPs

Since the deep-subwavelength HCGs on a PEC plane can support the propagation of spoof SPPs. Li et al. [159] further point out that HCGs in the form of a periodic array of radial dielectric blocks with high permittivity can support spoof-LSPs of TM form, which is further validated through a metamaterial approximation to capture all the resonant features both in 2D and 3D cases.

As shown in Fig. 7(a), a 2D closed textured surface consists of an HCG layer around a PEC cylindrical core. The HCGs structure stretching from the inner radius r to the outer radius R is a periodic dielectric array of two radial Blocks I and II with refractive indices n_{g1} and n_{g2} in one periodicity $d = 2\pi R/N = d_1 + d_2$. Blocks I and II have the same height $h = R - r$ and different widths d_1 and d_2. The subwavelength condition is satisfied. Block II is set as air with $n_{g2} = 1$ ($\varepsilon_{r2} = 1$, $\mu_{r2} = 1$), and Block I is set as a dielectric medium with high permittivity $n_{g1} = 2$ ($\varepsilon_{r1} = 4$, $\mu_{r1} = 1$). After the effective metamaterial approximation, the HCGs layer can be interpreted as a homogeneous equivalent medium of thickness $h = R - r$ as illustrated in Fig. 7(b). The effective parameters of the metamaterial in cylindrical coordinates can be obtained as [159]

$$\varepsilon_\varphi = \frac{d\varepsilon_{r1}\varepsilon_{r2}}{d_1\varepsilon_{r2} + d_2\varepsilon_{r1}}, \quad \varepsilon_\rho = \varepsilon_z = \frac{d_1\varepsilon_{r1} + d_2\varepsilon_{r2}}{d}. \tag{14}$$

In Fig. 7(c), HCGs-induced LSPs are distinct from MGs-induced ones in terms of the dispersion relation, normalized SCSs, and field distributions. This is a further expansion of Garcia-Vidal's theory for MGs-induced LSPs. Experimental results of surface field distributions in Figs. 7(d) and 7(e) further verified the HCGs-induced spoof-LSPs with 3D HCGs structure. It is remarked that HCGs-induced LSPs are a natural extension of the original concept of spoof-LSPs and can find potential applications in tunable designer-plasmonic sensors with ultrahigh Q-factor.

4. SPOOF SURFACE PLASMONS ARISING IN STRUCTURAL DISPERSION

Although spoof LSPs can mimic their natural counterparts in some aspects, they cannot be regarded as perfect low-frequency analogues of their optical version. This is because the effective permittivity of 2D corrugated PECs is not negative, and spoof LSPs do not decay spatially in the metallic corrugations

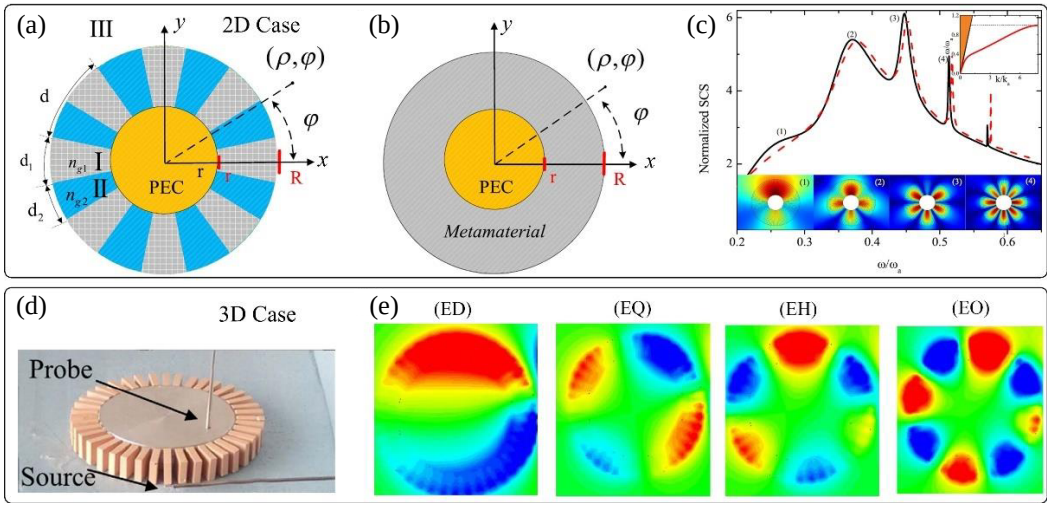

Figure 7. (a), (b) 2D HCGs-induced LSP model and effective medium approximation [159]. (c) The SCSs of the model in (a) and (b). (d), (e) 3D HCGs-induced LSP model and different resonance modes [159].

but resonate in the radial direction. As a result, the resonance properties of these modes rely heavily on the geometry of the structure, making many interesting properties of natural LSPs still elusive at low frequencies. Alternatively, it has been shown that low-frequency plasmonics can also be realized with structured dispersion in bounded waveguides [160–163]. In a couple of scenarios, this approach has been successfully applied to mimic SPPs and LSPs exhibiting spatial decay on both sides of the interface.

4.1. Structural Dispersion-Induced SPPs

The light-matter interaction in general exhibits frequency and wave vector dispersions. The frequency dispersion can be due to material dispersive response, which is the result of temporal characteristics of the polarization and magnetization densities in the materials. These dispersions, e.g., the well-known Drude and Lorentzian dispersions, may endow some materials with the negative real part of permittivity in certain frequency regimes, such as noble metals in the infrared and visible wavelengths. These ε-negative materials play an important role in the fields of plasmonic optics and photonic metamaterials [1–6], although they typically do suffer from strong losses. While the realization of artificial media with negative-ε response in the bulk is well established in the literature, at abrupt interfaces the typical metamaterial response typically deviates considerably from that of an ideal continuum mainly due to spatial dispersion effects and subsequent undesirable mode coupling [164, 165]. Thus, most metamaterial designs fail to imitate some of the salient and interesting features of SPPs in metal nanostructures at optics. A solution to overcome this limitation was reported in [160], wherein Giovampaola and Engheta put forward a parallel-plate waveguide (PPW) design for an effective negative-ε medium that retains the plasmonic features at material interfaces, even though the waveguide is filled with only positive-epsilon materials. The crucial novelty of that design is the insertion of tiny metallic wires at the interface between the two regions, preventing unwanted coupling from TM_1 to TE_1 mode, thus guaranteeing in this manner the exclusive propagation of the TE_1 mode and the suppression of spatially dispersive effects [164, 165]. The PPW in [160] has two regions with different positive-ε dielectrics, avoiding the dissipative losses from conventional negative-ε media. This method is more suitable for lower frequencies, allowing designers to employ positive-ε dielectrics and highly conductive metals for which the loss is low at these frequencies while achieving plasmonic features and a variety of plasmonic phenomena such as SPPs, LSPs resonance, plasmonic cloaking, and tunneling.

It is well known that if one considers a TE_{10} mode propagating in a PPW with PEC ceiling and

floor, one can express the relative effective permittivity of the TE_{10} mode as [160]

$$\varepsilon_e = \varepsilon_r - \frac{\lambda_0^2}{4a^2}, \tag{15}$$

where ε_r is the relative permittivity of the medium filling the waveguide, a the separation between the parallel metallic plates, and λ_0 the free-space wavelength. According to the above equation, one can design the PPW such that the effective permittivity of the mode is positive (effective-double-positive media), zero (effective-epsilon-near-zero), or negative (effective-epsilon-negative media). If one considers the field distribution for the TE_{10} mode [Fig. 8(a)], one will notice that in the middle plane parallel to the metallic plates of the PPW, both the electric and magnetic fields have only transverse components with respect to the direction of propagation of this TE_{10} mode. Therefore, if we restrict our observation to the middle plane of the PPW, the EM field distribution resembles the field distribution of a plane wave, which appears to propagate in an effective medium whose permittivity is equal to the effective permittivity of the mode inside the PPW [Fig. 8(b)]. It is worth highlighting that this effective permittivity exhibits the Drude dispersion, even if the filling material may be nondispersive. Since this dispersion is strongly related to waveguide effective structures, the resulting effective media can be called waveguide metamaterials [160] or effective surface plasmon polaritons (ESPPs) [161].

An important work has been put forward for comprehensively understanding the ESPPs in multilayer systems with theinsulator/metal/insulator (IMI) and themetal/insulator/metal (MIM) structures [163]. As shown in Figs. 8(c) and 8(d), a conventional rectangular waveguide with the cross-section dimensions $a \times b$ is filled with three-layer isotropic and homogeneous dielectrics. The dielectrics in Layer II ($-b/2 < y < -s$) and Layer III ($s < y < b/2$) are assumed to be the same ($\varepsilon_{r2} = \varepsilon_{r3}$ and $\mu_{r2} = \mu_{r3} = 1$). Two specific cases when $\varepsilon_{r2} = \varepsilon_{r3} > \varepsilon_{r1}$ and $\varepsilon_{r2} = \varepsilon_{r3} < \varepsilon_{r1}$ are mainly focused on. As described in Equation (15), the effective relative permittivity of the dielectric filling in the rectangular waveguide corresponding to TE_{m0} mode can be tuned to be either positive, zero, or negative by changing the operating frequency [39]. Then, the effective wave number would be $k_e = k_0\sqrt{\varepsilon_e}$. It is anticipated that effective surface confined modes can be supported at interface between Layers I and II, and interface between Layers I and III when $\mathrm{Re}(\varepsilon_{e1}) \cdot \mathrm{Re}(\varepsilon_{e2}) < 0$ and $\mathrm{Re}(\varepsilon_{e1}) < \mathrm{Re}(\varepsilon_{e3}) < 0$, where $\varepsilon_e = \varepsilon_{ri} - m^2\lambda_0^2/4a^2$, $i = 1, 2, 3$. By matching the boundary conditions, the dispersion relation for possible surface-confined modes is obtained as [163]

$$e^{-4k_{1y}s} = \frac{\left[\dfrac{k_{1y}}{\varepsilon_{e1}} + \dfrac{k_{2y}}{\varepsilon_{e2}}\tanh\left(k_{2y}t\right)\right]}{\left[\dfrac{k_{1y}}{\varepsilon_{e1}} - \dfrac{k_{2y}}{\varepsilon_{e2}}\tanh\left(k_{2y}t\right)\right]} \frac{\left[\dfrac{k_{1y}}{\varepsilon_{e1}} + \dfrac{k_{3y}}{\varepsilon_{e3}}\tanh\left(k_{3y}t\right)\right]}{\left[\dfrac{k_{1y}}{\varepsilon_{e1}} - \dfrac{k_{3y}}{\varepsilon_{e3}}\tanh\left(k_{3y}t\right)\right]}, \tag{16}$$

where $k_{iy}^2 = \beta^2 - k_i^2 + (m\pi/a)^2$, $m = 1, 2, 3, \ldots$. As stated above, Layer II and Layer III have the same permittivity $\varepsilon_{r2} = \varepsilon_{r3}$ ($\varepsilon_{e2} = \varepsilon_{e3}$) and thickness, and thus $k_{2y} = k_{3y}$. In this case, the dispersion relation (16) can be split into a pair of equations, namely [163]

$$\tanh\left(k_{1y}s\right) = -\frac{k_{2y}\varepsilon_{e1}}{k_{1y}\varepsilon_{e2}}\tanh\left(k_{2y}t\right), \tag{17a}$$

$$\tanh\left(k_{1y}s\right) = -\frac{k_{1y}\varepsilon_{e2}}{k_{2y}\varepsilon_{e1}}\coth\left(k_{2y}t\right). \tag{17b}$$

It can be observed that Equation (17a) describes modes of odd vector parity (E_z is odd, and H_x and E_y are even functions), while Equation (17b) describes modes of even vector parity (E_z is even, and H_x and E_y are odd functions). If we consider an extreme case when the thickness of the two claddings becomes infinite that $t \to \infty$ (the rectangular waveguide becomes a PPW with the separation a between the two plates), the two dispersion relations can be denoted by Equations (17a) and (17b) for the odd and even modes which are actually in the same form as those for the odd and even modes supported in sandwich structures in the optical regime [6] with only the replacement of $\varepsilon_i \to \varepsilon_{ei}$.

The results show that the ESPPs can be categorized into odd and even parities owing to the plasmon hybridization in a similar way to natural SPPs supported by the IMI and MIM heterostructures in the optical regime [68]. Long-ranging ESPPs can be realized by decreasing the thickness of the air layer of

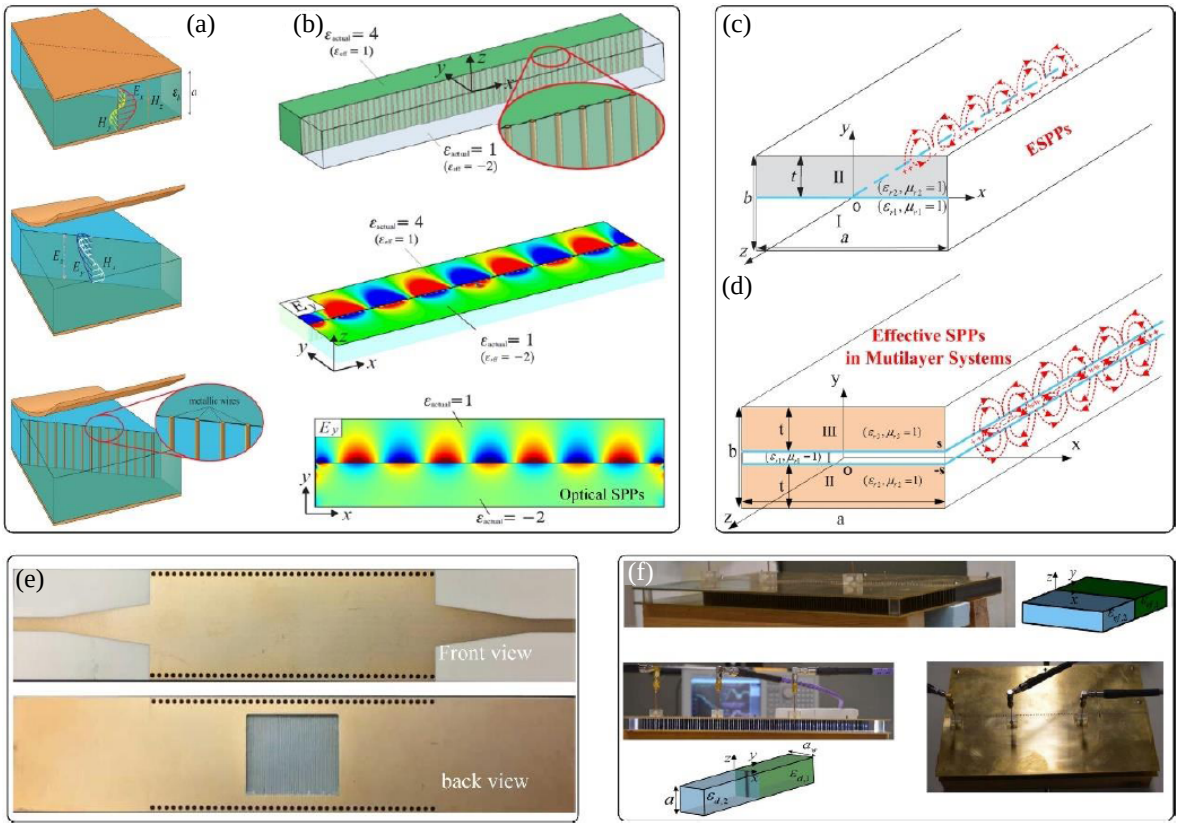

Figure 8. (a), (b) The ESPPs supported at the interface between two positive-ε dielectrics [160]. (c), (d) The ESPPs in multilayer systems with the IMI and the MIM structures [163]. (e), (f) Experimental demonstrations of the ESPPs in a double-layered SIW [161] and a PPW [162].

the effective IMI structure. And negative group velocity can also be achieved by tuning the geometrical dimensions of each layer for both the effective IMI and MIM structures [163]. In addition, the odd and even ESPPs modes in effective IMI/MIM structures are found to perfectly emulate the ultra-subwavelength confinement of SPPs in real IMI/MIM systems, which cannot be easily realized by the aforementioned MGs-induced spoof LSPs that a periodic array of grooves is needed with a depth on the order of one-quarter of wavelength.

The experimental demonstrations were conducted by Li et al. [Fig. 8(e)] in a plasmonic-type SIW [161] and by Prudencio et al. [Fig. 8(f)] in a plasmonic-type PPW [162] structure with positive-ε media, respectively. For MGs-SPPs, the guided wave is not truly localized at the interface. In contrast, ESPPs truly emulate the ultra-subwavelength confinement of spoof SPPs and are thus considered to be the perfect low-frequency counterpart of optical SPPs for both double-layered and multi-layered systems. Subsequent various well-known phenomena [160, 166, 167] and important applications [168–174] have been realized, including:

Effective Plasmonic Resonant Scattering and Cloaking: Fig. 9(a) shows a clear enhancement of the electric field surrounding a cylinder which is made of a dielectric with $\varepsilon_2 = 3.16$, where the waveguide around the cylinder is filled with a dielectric of $\varepsilon_1 = 5.16$. Such phenomenon confirms that the ESPP resonance of the cylindrical structure is caused by the proper value of effective permittivity of the cylinder $\varepsilon_{eff2} = -1$, but not by the wires or other factors. As shown in Fig. 9(b), a cylinder with radius $r_c = \lambda_0/30$ ($r_{cl} = 1.25r_c$) and actual dielectric of $\varepsilon_2 = 6.16$ embedded in a rectangular waveguide is filled with a medium with $\varepsilon_1 = 5.16$, thus a cylindrical cloak surrounding the cylinder with relative permittivity $\varepsilon_3 = 4.54$ was designed for effectively realizing the well-known plasmonic cloaking [160].

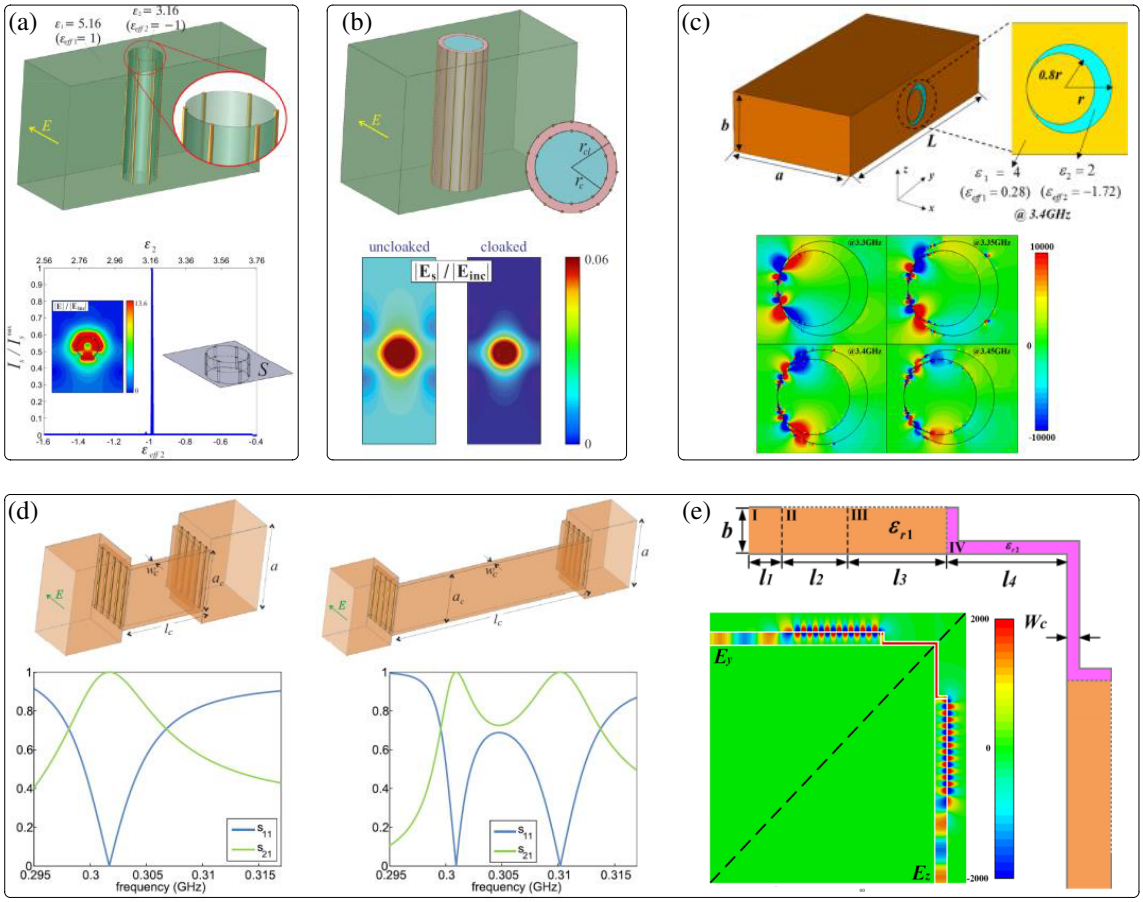

Figure 9. (a) Resonant scattering [160] and (b) plasmonic cloaking [160] with all positive-ε dielectrics inside a rectangular waveguide. (c) Broadband energy harvesting [166]. (d), (e) Tunneling of ESPPs [160, 167].

Efficient EM Energy Harvesting and Tunneling: As shown in Fig. 9(c), about 25% of EM energy has been harvested towards the singularity of the crescent thanks to the interaction between compressed ESPPs and the surrounding lossy dielectrics and metallic wires [166]. Figs. 9(d) and 9(e) show efficient EM energy tunneling by exploiting the ESPPs in an extremely narrow bent waveguide [160, 167].

Terahertz Subwavelength Imaging and Low-Loss Superlens: The low resolution and low contrast resulting from the diffraction limit and unwanted background illumination significantly hinder the extensive usage of current THz imaging technology. As shown in Fig. 10(a), a THz subwavelength imaging method capable of extracting only the edges and fine features of the targets is proposed based on the ESPPs [168], where the transmission channel for evanescent waves can be realized by hyperbolic metamaterials through periodically stacking dielectric layers. On this basis, high contrast edge detection with a resolution up to 0.1λ is achieved at THz wavelengths. Fig. 10(b) shows an extremely low hyperbolic metamaterial with independent effective permittivity components based on the ESPPs [169], which provides new ideas for the scenarios necessitating large permittivity coverage such as microwave and THz focus, super-resolution imaging, and EM cloaking. A low-loss superlens has been built with arbitrary materials at the desired frequency to enhance evanescent waves in a bounded PPW [170], as shown in Fig. 10(c). On the basis of this, a hyperbolic metamaterial without negative dielectrics is constructed and experimentally verified in the microwave range by directional propagation and imaging with a resolution of 0.087λ.

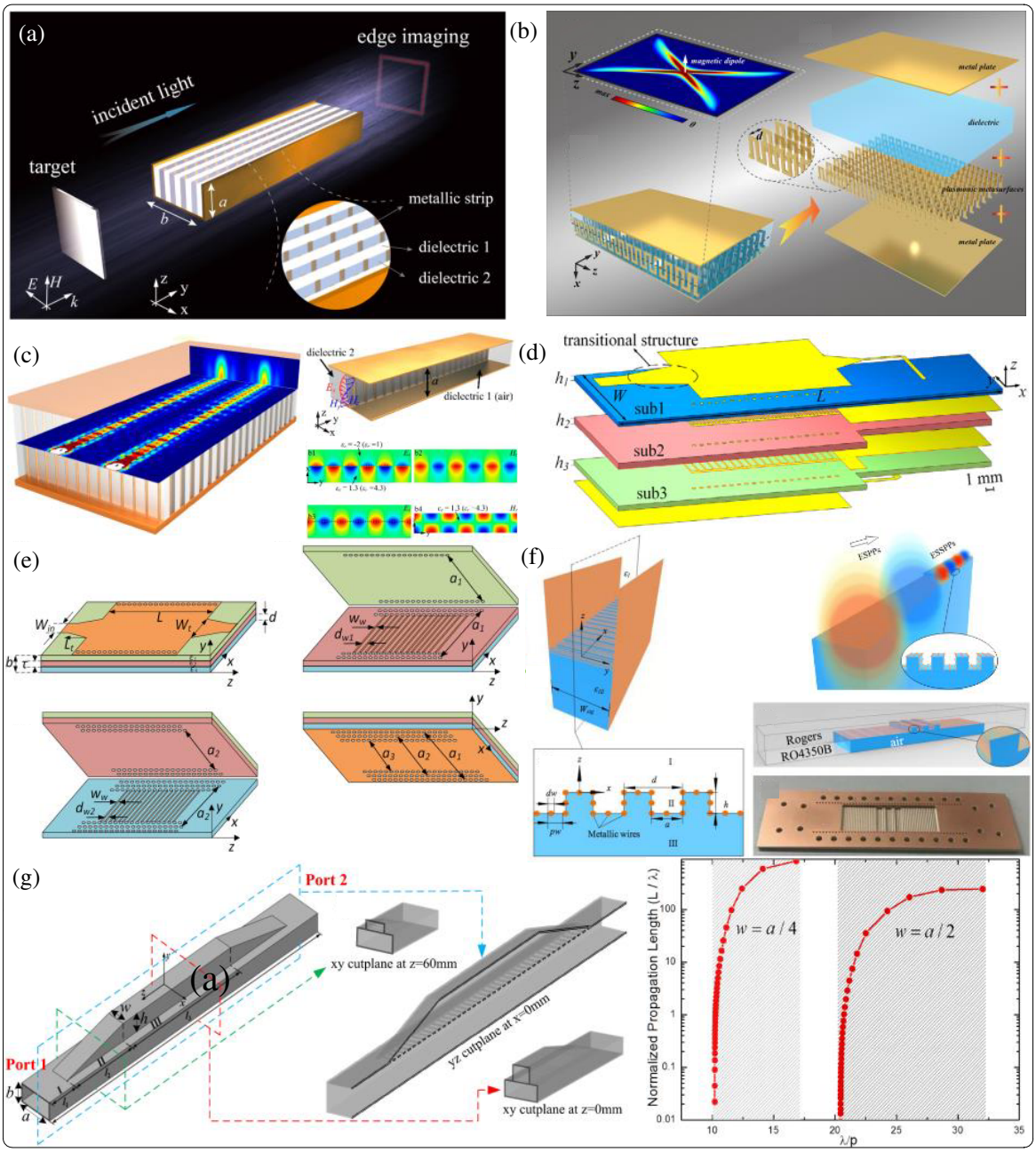

Figure 10. The ESPPs applications in (a) THz subwavelength edge imaging [168], (b) hyperbolic metamaterials for THz focus and super-resolution imaging [169], (c) low-loss superlens [170], (d) compact frequency splitter [171], (e) dual-band band-pass filters [172], (f) deeper confinement of ESPPs [173], (g) ultra-low loss waveguide [174].

Compact Frequency Splitter and Dual-Band Band-Pass Filter: In Fig. 10(d), a tunable dual-band band-pass frequency splitter based on ESPPs with a low profile and compact size is proposed [171]. By properly placing the substrates, two passbands can be flexibly tuned by changing the relative permittivity of the dielectric substrate and the lateral dimension of the SIW. In addition, two dual-band band-pass filters based on ESPPs are designed in Fig. 10(e) [172]. Both filters are realized by a three-layer SIW where each layer represents a sub-SIW structure with intrinsic effective

permittivity that depends on its width and filling dielectric material. Since three layers can provide two distinct ESPP propagations, the independent choice of geometrical parameters of *sub-SIWs* and/or the corresponding dielectric materials provides great freedom to arbitrarily position the passbands in the spectrum.

Enhancing Evanescent Waves and Ultralow Loss Transmission: To further enhance the field confinement of spoof SPPs, the ESPPs and MGs-induced SPPs are combined by hybridization and supported on a SIW platform [173], as shown in Fig. 10(f). The structural dispersion makes the wavelength of hybrid SPPs reach 1/18 as that of MGs-induced SPPs, indicating stronger field confinement and providing new possibilities to slowdown the wave propagation with controllable confinement with the obvious field confinement for the applications of device miniaturization and signal integrity. Fig. 10(g) shows a simple but robust scheme to dramatically reduce the transmission loss of the ESPPs by changing the lateral dimension of the upper layer of the waveguide, and thus an ultra-low loss of $|S_{21}|$ more than -0.5 dB from 6.7 GHz to 11.5 GHz plasmonic waveguide with tunable bandwidth can be easily obtained [174].

4.2. Structural Dispersion-Induced LSPs

In this section, let's revisit the structural dispersion of TE_1 mode in a bounded dielectric waveguide to realize effective LSPs (ELSPs). Specifically, we will review the physical mechanism behind ELSPs and show how sharp multipolar ELSP resonances can be introduced. In [175], Li et al. reveal that the effective permittivity of the air cylinder becomes negative, and multipolar resonances arise within a certain range of the spectrum, resembling the optical LSPs supported by a finite metal cylinder. Owing to dramatically suppressed metallic loss, the ELSP structure can support multipolar sharp plasmonic resonances, which are difficult to attain with natural plasmons at optical frequencies [5, 6].

As shown in Fig. 11(a), a cylinder of radius a and height d filled with isotropic and homogeneous dielectric (ε_{r2}, $\mu_{r2} = 1$) is placed in a PPW filled with an isotropic and homogeneous dielectric (ε_{r1}, $\mu_{r1} = 1$) [175]. An array of metallic wires is placed at the interface between these two dielectrics. Within the frequency range of interest, the PPW supports only TE_1 mode, and the whole structure can be considered as an effective medium. The propagation constant β of the TE_1 mode in the PPW can be expressed as $\beta = \sqrt{k^2 - k_c^2} = \sqrt{k^2 - (\pi/d)^2}$, where $k = k_0\sqrt{\varepsilon_r}$ is the wave number in the dielectric with relative permittivity ε_r, and $k_c = \pi/d$ is the cutoff wave number in the z-direction. When $k > k_c$, β is real, and the TE_1 mode is propagating. When $k < k_c$, β is imaginary, and the TE_1 mode becomes evanescent. From the effective medium perspective in Equation (15), effective permittivity ε_e can be tuned to be either positive or negative, mimicking real dielectrics or metals in the optical regime. To demonstrate the ELSPs can be supported at the interface between two positive dielectrics with effective permittivities of opposite signs in their real part $\mathrm{Re}(\varepsilon_{e1}) \cdot \mathrm{Re}(\varepsilon_{e2}) < 0$ within a certain frequency regime, and two types of ELSPs resembling a metallic rod in a dielectric or a dielectric inclusion in metallic structures are discussed [175].

The first category is to mimic a circular metallic rod immersed in a dielectric. It is imperative that $\varepsilon_{e1} > 0$ and $\varepsilon_{e2} < 0$. Therefore, the resonance frequencies of the ELSPs must be higher than $\omega_c|_{TE_1,\varepsilon_{r1}} = \pi c_0 \Big/ \left[d\sqrt{\mathrm{Re}(\varepsilon_{r1})}\right]$ and lower than $\omega_a = \pi c_0/d \cdot \sqrt{2/\mathrm{Re}(\varepsilon_{r1} + \varepsilon_{r2})}$, where ω_c is the cutoff frequency of the TE_1 mode in a PPW filled with the dielectric of relative permittivity ε_{r1}, and ω_a is the asymptotic frequency of the ESPPs that are supported at the interface between two semi-infinite dielectrics with permittivities ε_{e1} and ε_{e2}. When a TE_1 incident wave ($\vec{E}$ pointing along the y-direction) propagating along the $-x$ axis within the PPW, the electric and magnetic TE_1 fields have only y and z components, mimicking a plane wave. Thus, the analytical 2D SCS σ_{scs} of the cylinder can be obtained by applying the metamaterial approximation as [175]

$$\sigma_{scs} = \frac{4c_0}{\omega\sqrt{\varepsilon_{e1}}} \sum_{n=-\infty}^{+\infty} |a_n|^2 , \tag{18a}$$

in which

$$a_n = j^{-n} \frac{\sqrt{\dfrac{\varepsilon_{e1}}{\varepsilon_{e2}}} J_n(\beta_1 a) J_n'(\beta_2 a) - J_n'(\beta_1 a) J_n(\beta_2 a)}{H_n^{\prime(2)}(\beta_1 a) J_n(\beta_2 a) - \sqrt{\dfrac{\varepsilon_{e1}}{\varepsilon_{e2}}} J_n'(\beta_2 a) H_n^{(2)}(\beta_1 a)}, \tag{18b}$$

where $\beta_1 = \beta_0\sqrt{\varepsilon_{e1}}$, $\beta_2 = \beta_0\sqrt{\varepsilon_{e2}}$. The prime means differentiation with respect to the argument in parenthesis. If ε_{r1}, ε_{r2}, d, and a are all fixed, the resonance characteristics of multipolar ELSPs can be determined analytically by the SCS spectrum using Equation (18a) or simply calculated from the zeros of the denominator in Equation (18b).

The second category is to mimic a dielectric inclusion in metallic structures, and it is imperative that $\varepsilon_{e1} < 0$ and $\varepsilon_{e2} > 0$. Here, the materials in Regions I and II of Fig. 11(a) are simply switched by carrying out the substitutions $\varepsilon_{r1} \to \varepsilon_{r2}$, $\varepsilon_{r2} \to \varepsilon_{r1}$. In this case, the interface is expected to support void plasmons-like ELSPs whose resonance frequencies are also between ω_c and ω_a. When a specific case ($\varepsilon_{r1} = 1$, $\varepsilon_{r2} = 4$, $d = 22.86\,\text{mm}$, $a = 10.16\,\text{mm}$) is employed, the first four resonance frequencies corresponding to the di-, quadru-, hexa-, and octupolar modes can be calculated from the zeros of the denominator of Equation (18b), obtaining 3.734, 3.986, 4.075, and 4.104 GHz, respectively.

It should be noted that an important feature of ELSPs is that it can mimic the optical LSPs in a quasistatic limit. In other words, an ELSP structure can support only the dipolar mode by shrinking

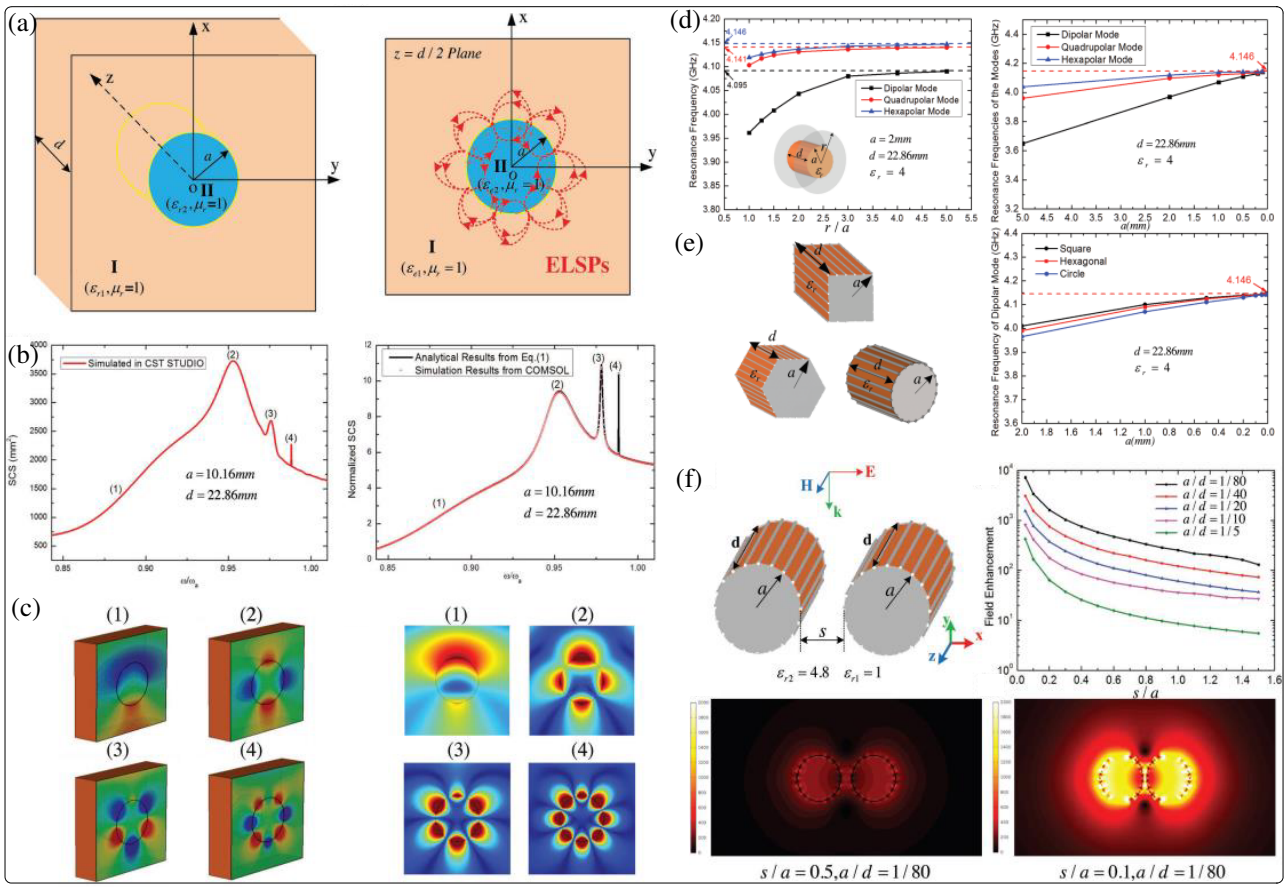

Figure 11. (a) The ELSPs supported at the interface between two positive-ε dielectrics [175]. (b) SCS spectrum of the ELSPs. (c) Magnetic field distributions of the ELSPs. (d) Evolution of the ELSPs' resonance frequencies with the decrease of the radius. (e) ELSP resonators with different cross-section shapes. (f) ELSP field enhancement [175].

the radius a into the deep subwavelength scale, which cannot be realized by the aforementioned MGs- and HCGs-induced LSPs. As shown in Figs. 11(d) and 11(e), for arbitrarily shaped ELSP structures, the resonance frequencies of all the ELSPs blueshift and degenerate into a single SCS peak where the dipolar mode dominates over higher-order resonances, and the quasistatic limit is reached. If $a \to 0$ in Equation (18b), $\varepsilon_{e2} = -\varepsilon_{e1}$ for the dipolar ELSP, recovering the well-known Fröhlich condition for optical LSPs. Compared with MGs-induced LSPs, ELSPs can achieve stronger field enhancement between the two adjacent structures. Fig. 11(f) shows that the peak field enhancement at the dipolar resonance increases with shrinking structural dimensions and reaches a value > 800 when the dimension a is reduced below 2 mm. These findings show that ELSP modes are quite sensitive to the background refractive index but relatively robust to the size and shape of the resonator. It is worth highlighting that the ELSPs open up a new avenue for designer localized surface waves at low frequencies and can find applications in the miniaturization of microwave resonators, filters, EM energy harvesting, and THz biosensors [175].

Miniaturization of Resonators and Filters: By virtue of the insensitiveness of the ELSPs resonator's dipolar mode resonance frequency to the variations of its cross-sectional dimensions and shape [Fig. 12(a)], the occupied area of the filter can be significantly miniaturized, and the unloaded quality factor of the ELSPs resonator can be flexibly tuned and adjusted to be much larger than that of conventional microstrip and SIW resonators [176]. Based on this feature, an ultracompact and miniaturized dual-mode cavity filter [177, 178] constructed by an 18 mm $\times$ 18 mm $\times$ 18 mm cube cavity and a cylindrical ELSPs resonator was designed, as shown in Fig. 12(b), in which two Sub-6G plasmonic bandpass filters centered at 3.3 and 3.4 GHz with the size of only 0.006 and $0.021\lambda_0^2$ are designed and implemented [177].

Broadband and High Sensitivity Sensor: Liquid permittivity measurement and testing become more and more common and important in recent highly integrated systems. An ultra-compact microwave sensor of $0.008\lambda_0^2$ based on the ELSP resonance was designed for complex permittivity measurement of aqueous ethanol solution in [179], as shown in Fig. 12(d). The sensitivity of the sensor is dramatically enhanced thanks to the strong EM coupling and enhancement of the ELSP in a deep-subwavelength scale. The complex permittivity of aqueous ethanol solution with an ethanol concentration of 0%–90% was successfully predicted with high sensitivity of 0.57%.

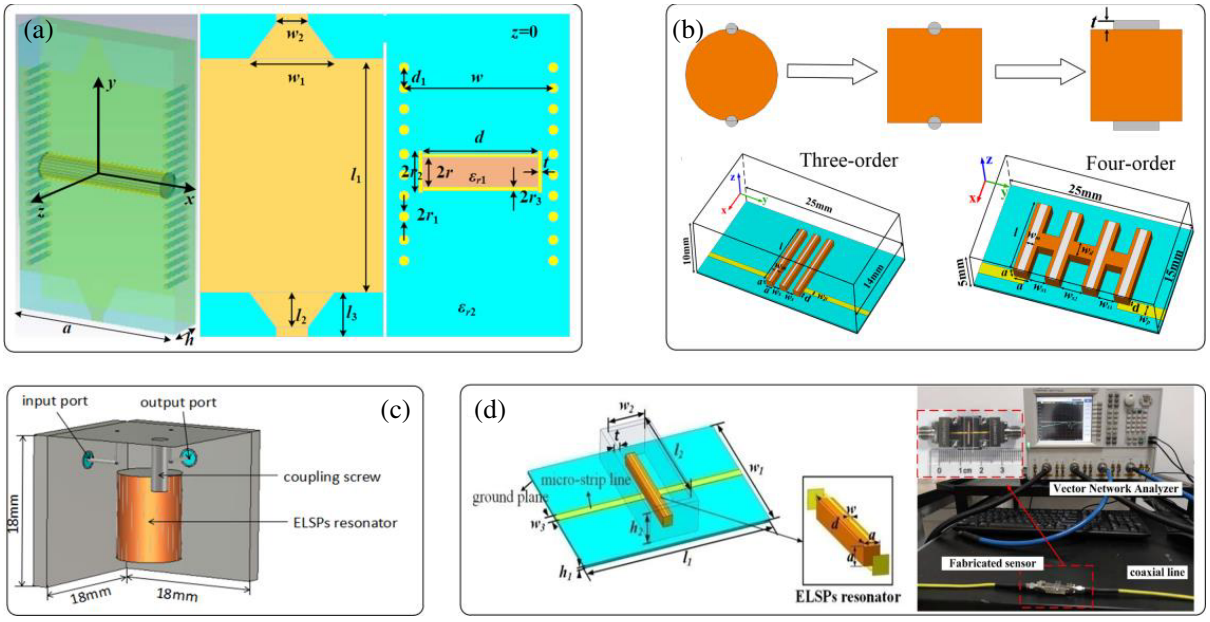

Figure 12. (a) Efficient excitation of dispersion-induced ELSPs in a SIW. (b) Ultracompact bandpass filters. (c) Dual-mode cavity filter. (d) Broadband and high sensitivity sensor.

5. SUMMARY AND OUTLOOK

In this paper, we have reviewed the fundamentals of three spoof surface plasmons arising in MGs, HCGs, and structural dispersion waveguides in the lower frequencies. The review focuses primarily on the basic concept, design method, efficient experiment realization, and their great applications in microwave and THz engineering. We have outlined how spoof surface plasmons enable the existence of the propagation and localized surface EM modes under three different mechanisms. Their geometrical origin, as well as their properties, can be described with the coupled-mode formalism and effective metamaterial approximations. We see the exotic characteristics of the spoof surface plasmons in terms of flexible dispersion and propagation characteristics, configurable localized field confinement, and their great potential for future circuits with high integration, compact size, and excellent performance.

Since Pendry et al. proposed the concept of spoof plasmonics, it has been developed to be an independent research branch in the broad field of metamaterials in parallel to negative refraction and invisibility cloaking. Various descriptions and designs have been proposed to characterize and control the spoof plasmon modes at the subwavelength scale. Thanks to the subwavelength field confinement and low absorption loss, spoof surface plasmons are deemed to be promising information carriers for future subwavelength THz and optical circuitry. In view of the present development trends in spoof plasmons, we anticipate hereinafter that in the near future this field will develop toward both fundamental and practical directions.

1) For MGs-induced spoof plasmons, some interesting phenomena that are challenging to demonstrate and observe directly, such as anomalous plasmonic modes [180], compacted dimensions on singular plasmonic surfaces [181, 182], quantum spin Hall effect [183], generalized Kerker effect [184–187], and spoof magnetic surface plasmons [188] can be experimentally demonstrated on the spoof plasmonic platform. Moreover, a development direction that is very worth paying attention to is the design of active flexible plasmonic components and circuits. Actually, at microwave frequencies, active chips with various functionalities are available using semiconductor technology. Exploration should be conducted to identify more efficient ways to load active chips in the spoof plasmon circuits to achieve high-performance indispensable modules such as oscillators, mixers, frequency multipliers, nonlinear harmonic generators, and amplifiers, as well as a large-scale wireless communication system [113–124]. Spoof plasmonics is particularly useful in the THz regime where high-integrated waveguide components with superior performance are still lacking. For example, it can help design better next-generation THz electronics and sensing, as currently happening in complementary metal-oxide-semiconductor (CMOS) compatible THz on-chip circuitry to improve the integrity and sensitivity of the signal in the on-chip communication system. Another more promising development direction is sensing [189–192]. The widespread use of THz spectroscopy in sensing technology is greatly hindered by the low power of sources and poor sensitivity of detectors. However, these limitations can be circumvented by exploiting the strongly confined EM fields provided by spoof plasmon metamaterials [189, 190]. Through the field enhancement provided by spoof surface plasmon modes, light-matter interactions can be strengthened, which allows for the detection of small changes in the dielectric environment of the THz metamaterial, for example, utilizing spoof plasmons metamaterials to achieve the non-Hermitian spectral degeneracies, known as exceptional points [193], in a microwave or THz whispering gallery mode micro-toroid cavity for sensing applications.

2) For HCGs-induced spoof plasmons, although the current research work is relatively scarce, thanks to the non-metallization feature, various interesting physical phenomena, and the essential integrated optoelectronics devices and circuits [194] can be realized on the HCGs-based spoof plasmonic platform. For example, various designs can be conducted to yield broadband, high-reflectivity mirrors for light incident in surface-normal direction and at a glancing angle [195], ultrahigh-Q resonators with surface-normal output [196], high-Q metagrating supporting bound states in the continuum [197], planar high focusing power reflectors and lenses [198], and ultralow loss hollow-core waveguides [196]. The HCGs-induced spoof plasmonic will be a more promising platform for integrated optoelectronics with applications for vertical-cavity surface-emitting lasers, filters, waveguides, sensors, detectors, interconnects, and delay lines [199–201].

3) For structural dispersion-induced spoof plasmons, an interesting concept of waveguide metatronics [202], which is an advanced form of optical metatronics that uses structural dispersion in waveguides to obtain the materials and structures required to construct the lumped circuitry, is

a promising development direction. The waveguide metatronics can extend the concepts of optical metatronics to frequency ranges where there are no natural plasmonic materials available and can help design the epsilon-negative (ENG) [203], epsilon-near-zero (ENZ) [204, 205], or both ENG and ENZ media [206] using conventional positive-dielectric materials. Moreover, structural dispersion-based hyperbolic metamaterial [168, 169] is another important development point. In this way, such as negative refraction [207], superlens [170], and non-Hamiltonian topological thermal insulators [208] can be realized only with positive permittivity materials. As perfect low-frequency analogues of optical SPPs and LSPs, some interesting physical effects that are challenging to demonstrate and observe directly at high frequencies, such as nonlocal effect [209, 210], plasmon hybridization [152, 211], broadband EM energy harvesting [166, 212] can be experimentally demonstrated at lower frequencies.

ACKNOWLEDGMENT

This work is supported in part by the National Natural Science Foundation of China (Nos. 61771238, 61871215, 61701246); State Key Laboratory of Millimeter Waves (No. K202209); Six talent peaks project in Jiangsu Province (No. 2018-GDZB-009).

Conflict of Interest

The authors declare no conflict of interest.

Data Availability Statement

The data that supports the plots within this letter and other findings of this study are available from the corresponding author upon reasonable request.

REFERENCES

1. Raether, H., *Surface Plasmons on Smooth and Rough Surfaces and on Gratings*, Springer, 1988.
2. Economou, E. N., "Surface plasmons in thin films," *Phys. Rev.*, Vol. 182, No. 2, 539–554, 1969.
3. Ritchie, R. H., "Surface plasmons in solids," *Surface Science*, Vol. 34, No. 1, 1–19, 1973.
4. Murray, W. A. and W. L. Barnes, "Plasmonic materials," *Adv. Mater.*, Vol. 19, No. 22, 3771–82, 2007.
5. Barnes, W. L., A. Dereux, and T. W. Ebbesen, "Surface plasmon subwavelength optics," *Nature*, Vol. 424, No. 6950, 824–830, 2003.
6. Maier, S. A., *Plasmonics Fundamentals and Applications*, Springer, Boston, MA, 2007.
7. Huidobro P. A., A. I. Fernández-Domínguez, J. B. Pendry, et al., *Spoof Surface Plasmon Metamaterials*, Cambridge University Press, 2018.
8. Gramotnev, D. K. and S. I. Bozhevolnyi, "Plasmonics beyond the diffraction limit," *Nat. Photon.*, Vol. 4, No. 2, 83–91, 2010.
9. Maier, S. A. and H. A. Atwater, "Plasmonics: Localization and guiding of electromagnetic energy in metal/dielectric structures," *J. Appl. Phys.*, Vol. 98, No. 1, 011101, 2005.
10. Ozbay, E., "Plasmonics: Merging photonics and electronics at nanoscale dimensions," *Science*, Vol. 311, No. 5758, 189–193, 2006.
11. Novotny, L., "Effective wavelength scaling for optical antennas," *Phys. Rev. Lett.*, Vol. 98, No. 26, 266802, 2007.
12. Bryant, G. W., F. J. García de Abajo, and J. Aizpurua, "Mapping the plasmon resonances of metallic nanoantennas," *Nano Lett.*, Vol. 8, No. 2, 631–636, 2008.
13. Schuller, J. A., E. S. Barnard, W. Cai, et al., "Plasmonics for extreme light concentration and manipulation," *Nature Mater.*, Vol. 9, No. 3, 193–204, 2010.
14. Fan, J. A., C. Wu, K. Bao, et al., "Self-assembled plasmonic nanoparticle clusters," *Science*, Vol. 328, No. 5982, 1135–8, 2010.

15. Ozbay, E., "Plasmonics: Merging photonics and electronics at nanoscale dimensions," *Science*, Vol. 311, No. 5758, 189–193, 2006.
16. Anker, J. N., W. P. Hall, O. Lyandres, et al., "Biosensing with plasmonic nanosensors," *Nature Mater.*, Vol. 7, 442, 2008.
17. Kabashin, A. V., P. Evans, S. Pastkovsky, et al., "Plasmonic nanorod metamaterials for biosensing," *Nature Mater.*, Vol. 8, 867, 2009.
18. Flatgen, G., K. Krischer, B. Pettinger, et al., "Two-dimensional imaging of potential waves in electrochemical systems by surface plasmon microscopy," *Science*, Vol. 269, 668, 1995.
19. Ebbesen, T. W., H. J. Lezec, H. F. Ghaemi, et al., "Extraordinary optical transmission through sub-wavelength hole arrays," *Nature*, Vol. 391, 667, 1998.
20. Martín-Moreno, L., F. J. García-Vidal, H. J. Lezec, et al., "Theory of extraordinary optical transmission through subwavelength hole arrays," *Phys. Rev. Lett.*, Vol. 86, 1114, 2001.
21. Zhang, S., D. A. Genov, Y. Wang, et al., "Plasmon-induced transparency in metamaterials," *Phys. Rev. Lett.*, Vol. 101, 047401, 2008.
22. Kekatpure, R. D., E. S. Barnard, W. Cai, et al., "Phase-coupled plasmon-induced transparency," *Phys. Rev. Lett.*, Vol. 104, 243902, 2010.
23. Gobau, G., "Surface waves and their application to transmission lines," *J. Appl. Phys.*, Vol. 21, 1119, 1950.
24. Mills, D. L. and A. A. Maradudin, "Surface corrugation and surface-polariton binding in the infrared frequency range," *Phys. Rev. B*, Vol. 39, 1569, 1989.
25. Munk, B. A., *Frequency Selective Surfaces: Theory and Design*, Wiley, New York, NY, 2000.
26. Zenneck, J., "Propagation of plane electromagnetic waves along a plane conducting surface," *Ann. Phys.*, Vol. 23, No. 1, 846, 1907.
27. Sommerfeld, A., "Propagation of electrodynamic waves along a cylindric conductor," *Ann. Phys. und Chemie*, Vol. 67, 233, 1899.
28. Ulrich, R. and M. Tacke, "Submilimeter waveguiding on periodic metal structure," *Appl. Phys. Lett.*, Vol. 22, 251, 1973.
29. Pendry, J. B., L. Martín-Moreno, and F. J. García-Vidal, "Mimicking surface plasmons with structured surfaces," *Science*, Vol. 305, No. 5685, 847–848, 2004.
30. García-Vidal, F. J., L. Martín-Moreno, and J. B. Pendry, "Surfaces with holes inthem: New plasmonic metamaterials," *J. Opt. A: P. Appl. Opt.*, Vol. 7, No. 2, S97–S101, 2005.
31. Pors, A., E. Moreno, L. Martin-Moreno, et al., "Localized spoof plasmons arise while texturing closed surfaces," *Phys. Rev. Lett.*, Vol. 108, 223905, 2012.
32. Engheta, N. and R. W. Ziolkowski, *Metamaterials: Physics and Engineering Explorations*, Wiley, New York, 2006.
33. Hibbins, A. P., B. R. Evans, and J. R. Sambles, "Experimental verification of designer surface plasmons," *Science*, Vol. 308, No. 5722, 670–672, 2005.
34. Hibbins, A. P., E. Hendry, M. J. Lockyear, and J. R. Sambles, "Prism coupling to 'designer' surface plasmons," *Opt. Express*, Vol. 16, 20441, 2008.
35. Lockyear, M. J., A. P. Hibbins, and J. R. Sambles, "Microwave surface-plasmon-like modes on thin metamaterials," *Phys. Rev. Lett.*, Vol. 102, 073901, 2009.
36. Hibbins, A. P., M. Lockyear, I. Hooper, and J. Sambles, "Waveguide arrays as plasmonic metamaterials: Transmission below cutoff," *Phys. Rev. Lett.*, Vol. 96, No. 7, 073904, 2006.
37. Wood, R. W., "On a remarkable case of uneven distribution of light in a diffraction grating spectrum," *Philos. Mag.*, Vol. 4, No. 21, 396–402, 1902.
38. Williams, C. R., S. R. Andrews, S. A. Maier, et al., "Highly confined guiding of terahertz surface plasmon polaritons on structured metal surfaces," *Nat. Photon.*, Vol. 2, No. 3, 175–179, 2008.
39. Zhao, W., O. M. Eldaiki, R. Yang, and Z. Lu, "Deep subwavelength waveguiding and focusing based on designer surface plasmons," *Opt. Express*, Vol. 18, No. 20, 21498–21503, 2010.

40. Zhu, W., A. Agrawal, and A. Nahata, "Planar plasmonic terahertz guided-wave devices," *Opt. Express*, Vol. 16, 6216, 2008.
41. Qiu, M., "Photonic band structures for surface waves on structured metal surfaces," *Opt. Express*, Vol. 13, 7583, 2005.
42. Gao, Z., L. Wu, F. Gao, et al., "Spoof plasmonics: From metamaterial concept to topological description," *Adv. Mater.*, Vol. 30, 1706683, 2018.
43. Gómez-Rivas, J., M. Kuttge, P. H. Bolivar, et al., "Propagation of surface plasmon polaritons on semiconductor gratings," *Phys. Rev. Lett.*, Vol. 93, No. 25, 256804, 2004.
44. García de Abajo, F. J. and J. J. Sáenz, "Electromagnetic surface modes in structured perfect-conductor surfaces," *Phys. Rev. Lett.*, Vol. 95, No. 2, 233901, 2005.
45. Yu, N. F., Q. J. Wang, M. A. Kats, et al., "Designer spoof surface plasmon structures collimate terahertz laser beams," *Nature Mater.*, Vol. 9, No. 9, 730–735, 2010.
46. Maier, S. A., S. A. Andrews, L. Martín-Moreno, et al., "Terahertz surface plasmon-polariton propagation and focusingon periodically corrugated metal wires," *Phys. Rev. Lett.*, Vol. 97, No. 17, 176805, 2006.
47. Fernández-Domínguez, A. I., L. Martín-Moreno, F. J. García-Vidal, et al., "Spoof surface plasmon polariton modes propagating along periodically corrugated wires," *IEEE J. Sel. Top Quant. Elect.*, Vol. 14, 1515, 2008.
48. Fernández-Domínguez, A. I., C. R. Williams, F. J. García-Vidal, et al., "Terahertz surface plasmon polaritons on a helically grooved wire," *Appl. Phys. Lett.*, Vol. 93, No. 14, 141109, 2008.
49. Ruting, F., A. I. Fernández-Dominguez, L. Martín-Moreno, et al., "Subwavelength chiral surface plasmons that carry tunable orbital angular momentum," *Phys. Rev. B*, Vol. 86, 075437, 2012.
50. Liu, L. L., Z. Li, P. P. Ning, et al., "Deep-subwavelength guiding and superfocusing of spoof surface plasmon polaritons on helically grooved metal wire," *Plasmonics*, Vol. 11, No. 2, 359–364, 2016.
51. Wood, J. J., L. A. Tomlinson, O. Hess, S. A. Maier, and A. I. Fernández-Dominguez, "Spoof plasmon polaritons in slanted geometries," *Phys. Rev. B*, Vol. 85, 075441, 2012.
52. Ruan, Z. C. and M. Qiu, "Slow electromagnetic wave guided in subwavelength region along one-dimensional periodically structured metal surface," *Appl. Phys. Lett.*, Vol. 90, 201906, 2007.
53. Novikov, I. V. and A. A. Maradudin, "Channel polaritons," *Phys. Rev. B*, Vol. 66, 035403, 2002.
54. Fernández-Domínguez, A. I., E. Moreno, L. Martín-Moreno, and F. J. García-Vidal, "Guiding terahertz waves along subwavelength channels," *Phys. Rev. B*, Vol. 79, No. 23, 233104, 2009.
55. Jiang, T., L. F. Shen, J. J. Wu, et al., "Realization of tightly confined channel plasmon polaritons at low frequencies," *Appl. Phys. Lett.*, Vol. 99, No. 26, 261103, 2011.
56. Gao, Z., L. F. Shen, and X. Zheng, "Highly-confined guiding of terahertz waves along subwavelength grooves," *IEEE Photon. Tech. Lett.*, Vol. 24, No. 15, 1343–5, 2012.
57. Li, X., T. Jiang, L. F. Shen, and D. X. Ye, "Subwavelength guiding of channel plasmon polaritons by textured metallic grooves at telecom wavelengths," *Appl. Phys. Lett.*, Vol. 102, No. 3, 031606, 2013.
58. Fernández-Domínguez, A. I., E. Moreno, L. Martín-Moreno, and F. J. García-Vidal, "Terahertz wedge plasmon polaritons," *Opt. Lett.*, Vol. 34, No. 13, 2063–2065, 2009.
59. Gao, Z., X. Zhang, and L. F. Shen, "Wedge mode of spoof surface plasmon polaritons at terahertz frequencies," *J. Appl. Phys.*, Vol. 108, No. 11, 113104, 2010.
60. Moreno, E., S. G. Rodrigo, S. I. Bozhevolnyi, et al., "Guiding and focusing of electromagnetic fields with wedge plasmon polaritons," *Phys. Rev. Lett.*, Vol. 100, No. 2, 023901, 2008.
61. Martín-Cano, D., M. L. Nesterov, A. I. Fernández-Domínguez, et al., "Domino plasmons for subwavelength terahertz circuitry," *Opt. Express*, Vol. 18, No. 2, 754–764, 2010.
62. Ma, Y. G., L. Lan, S. M. Zhong, and C. K. Ong, "Experimental demonstration of subwavelength domino plasmon devices for compact high-frequency circuit," *Opt. Express*, Vol. 19, No. 22, 21189, 2011.

63. Martín-Cano, D., O. Quevedo-Teruel, E. Moreno, et al., "Waveguided spoof surface plasmons with deep subwavelength lateral confinement," *Opt. Lett.*, Vol. 36, No. 23, 4635–4637, 2011.
64. Brock, E. M. G., E. Hendry, and A. P. Hibbins, "Subwavelength lateral confinement of microwave surface waves," *Appl. Phys. Lett.*, Vol. 99, No. 5, 051108, 2011.
65. Kats, M. A., D. Woolf, R. Blanchard, et al., "Spoof plasmon analogue of metal-insulator-metal waveguides," *Opt. Express*, Vol. 19, No. 16, 14860–14870, 2011.
66. Woolf, D., M. Kats, and F. Capasso, "Spoof surface plasmon waveguide forces," *Opt. Lett.*, Vol. 39, No. 3, 517–520, 2014.
67. Quesada, R., D. Martín-Cano, F. J. García-Vidal, and J. Bravo-Abad, "Deep subwavelength negative-index waveguiding enabled by coupled conformal surface plasmons," *Opt. Lett.*, Vol. 39, No. 10, 2990, 2014.
68. Chen, N. C., C. Y. Lu, Y. L. Huang, et al., "Properties of coupled surface plasmon-polaritons in metal-dielectric-metal structures," *J. Appl. Phys.*, Vol. 112, 033111, 2012.
69. Shen, X. P., T. J. Cui, D. Martin-Cano, and F. J. Garcia-Vidal, "Conformal surface plasmons propagating on ultrathin and flexible films," *Proceedings of the National Academy of Sciences of the United States of America-PNAS*, Vol. 110, No. 1, 40–45, 2013.
70. Shen, X. P. and T. J. Cui, "Planar plasmonic metamaterial on a thin film with nearly zero thickness," *Appl. Phys. Lett.*, Vol. 102, No. 21, 14–18, 2013.
71. Gan, Q. Q., Z. Fu, Y. J. Ding, and F. J. Bartoli, "Ultrawide-bandwidth slow-light system based on THz plasmonic graded metallic grating structures," *Phys. Rev. Lett.*, Vol. 100, 256803, 2008.
72. Tang, Y. B., Z. C. Wang, L. Wosinski, et al., "Highly efficient nonuniform grating coupler for silicon-on-insulator nanophotonic circuits," *Opt. Lett.*, Vol. 35, No. 8, 1290–1292, 2010.
73. Liu, X., Y. Feng, K. Chen, et al., "Planar surface plasmonic waveguide devices based on symmetric corrugated thin film structures," *Opt. Express*, Vol. 22, No. 17, 20107, 2014.
74. Zhou, Y. J., Q. Jiang, and T. J. Cui, "Bidirectional bending splitter of designer surface plasmons," *Appl. Phys. Lett.*, Vol. 99, No. 11, 111904, 2011.
75. Gao, X., J. H. Shi, X. P. Shen, et al., "Ultrathin dual-band surface plasmonic polariton waveguide and frequency splitter in microwave frequencies," *Appl. Phys. Lett.*, Vol. 102, No. 15, 1–5, 2013.
76. Liu, X., Y. Feng, B. Zhu, et al., "High-order modes of spoofsurface plasmonic wave transmission on thin metal film structure," *Opt. Express*, Vol. 21, No. 25, 31155–31165, 2013.
77. Sun, S. L., Q. He, S. Xiao, Q. Xu, X. Li, and L. Zhou, "Gradient-index metasurfaces as a bridge linking propagating waves and surface waves," *Nature Mater.*, Vol. 11, No. 5, 426–431, 2012.
78. Ma, H. F., X. P. Shen, Q. Cheng, et al., "Broadband and high efficiency conversion from guided waves to spoof surface plasmon polaritons," *Laser Photon. Rev.*, Vol. 8, No. 1, 146–151, 2014.
79. Zhang, W. J., G. Q. Zhu, L. G. Sun, and F. J. Lin, "Trapping of surface plasmon wave through gradient corrugated strip with underlayer ground and manipulating its propagation," *Appl. Phys. Lett.*, Vol. 106, 021104, 2015.
80. Liu, L. L., Z. Li, B. Z. Xu, et al., "Dual-band trapping of spoof surface plasmon polaritons and negative group velocity realization through microstrip line with gradient holes," *Appl. Phys. Lett.*, Vol. 107, No. 20, 2015.
81. Gao, X., L. Zhou, Z. Liao, et al., "An ultra-wideband surface plasmonic filter in microwave frequency," *Appl. Phys. Lett.*, Vol. 104, No. 19, 17–22, 2014.
82. Liu, L. L., Z. Li, B. Z. Xu, et al., "Fishbone-like high-efficiency low-pass plasmonic filter based on double-layered conformal surface plasmons," *Plasmonics*, Vol. 12, No. 2, 439–444, 2017.
83. Zhang, H. C., L. Liu, P. H. He, et al., "A wide-angle broadband converter: From odd-mode spoof surface plasmon polaritons to spatial waves," *IEEE Trans. on Antennas and Propa.*, Vol. 67, No. 12, 7425–7432, 2019.
84. Zhou, S. Y., S. W. Wong, and J. Y. Lin, "Four-way spoof surface plasmon polaritons splitter/combiner," *IEEE Ant. and Wire. Prop. Lett.*, Vol. 29, No. 2, 98–100, 2019.
85. Tang, W. X., H. C. Zhang, H. F. Ma, et al., "Concept, theory, design, and applications of spoof surface plasmon polaritons at microwave frequencies," *Adv. Opt. Mater.*, 1800421, 2018.

86. Xu, J., Z. Li, L. L. Liu, et al., "Low-pass plasmonic filter and its miniaturization based on spoof surface plasmon polaritons," *Opt. Comm.*, Vol. 372, 155–159, 2016.
87. Xu, B. Z., Z. Li, L. L. Liu, et al., "Bandwidth tunable microstrip band-stop filters based on localized spoof surface plasmons," *J. Opt. Soc. America B*, Vol. 33, No. 7, 1388–1391, 2016.
88. Li, Z., J. Xu, C. Chen, et al., "Coplanar waveguide wideband band-stop filter based on localized spoof surface plasmons," *Appl. Opt.*, Vol. 55, No. 36, 10323–10328, 2016.
89. Kianinejad, A., Z. N. Chen, and C. W. Qiu, "Design and modeling of spoof surface plasmon modes-based microwave slow-wave transmission line," *IEEE Trans. Micro. Theory and Tech.*, Vol. 63, No. 6, 1817–1825, 2015.
90. Kianinejad, A., Z. N. Chen, and C. W. Qiu, "Low-loss spoof surface plasmon slow-wave transmission lines with compact transition and high isolation," *IEEE Trans. Micro. Theory and Tech.*, Vol. 64, No. 10, 3078–3086, 2016.
91. Wu, J. J., D. J. Hou, and K. X. Liu, "Differential microstrip lines with reduced crosstalk and common mode effect based on spoof surface plasmon polaritons," *Opt. Express*, Vol. 22, No. 22, 26777–26787, 2014.
92. Zhang, H. C., T. J. Cui, Q. Zhang, et al., "Breaking the challenge of signal integrity using time-domain spoof surface plasmon polaritons," *ACS Photon.*, Vol. 2, No. 9, 1333–1340, 2015.
93. Zhao, S. M., H. C. Zhang, L. L. Liu, et al., "A novel low-crosstalk driveline based on spoof surface plasmon polaritons," *IEEE Access*, Vol. 7, 30702–30707, 2019.
94. Gao, X. X., H. C. Zhang, P. H. He, et al., "Crosstalk suppression based on mode mismatch between spoof SPP transmission line and microstrip," *IEEE Trans. on Compon., Pack. and Manuf. Techn.*, Vol. 9, No. 11, 2267–2275, 2019.
95. Wang, M. N., M. Tang, H. C. Zhang, et al., "Crosstalk noise suppression between single and differential transmission lines using spoof surface plasmon polaritons," *IEEE Trans. on Compon., Pack. and Manuf. Techn.*, Vol. 10, No. 8, 1367–1374, 2020.
96. Liu, L. L., Z. Li, C. Q. Gu, et al., "Multi-channel composite spoof surface plasmon polaritons propagating along periodically corrugated metallic thin films," *J. Appl. Phys.*, Vol. 116, 013501, 2014.
97. Yang, B. J. and Y. J. Zhou, "Compact four-way wavelength demultiplexers based on conformal surface plasmon waveguides," *Jpn. J. Appl. Phys.*, Vol. 54, 112201, 2015.
98. Yang, B. J. and Y. J. Zhou, "Wavelength filtering and demultiplexing devices based on ultrathin corrugated MIM waveguides," *J. Modern Opt.*, Vol. 63, No. 9, 874–880, 2016.
99. Kianinejad, A., Z. N. Chen, L. Zhang, et al., "Spoof plasmon-based slow-wave excitation of dielectric resonator antennas," *IEEE Trans. Ant. and Prop.*, Vol. 64, No. 6, 2094–2099, 2016.
100. Han, Y. J., Y. F. Li, H. Ma, et al., "Multibeam antennas based on spoof surface plasmon polaritons mode coupling," *IEEE Trans. Ant. and Prop.*, Vol. 65, No. 3, 1187–1192, 2017.
101. Li, Z., C. Chen, L. L. Liu, et al., "Tunable spoof surface plasmons bulleye antenna," *Plasmonics*, Vol. 13, No. 2, 697–703, 2018.
102. Han, Y. J., J. F. Wang, S. H. Gong, et al., "Low RCS antennas based on dispersion engineering of spoof surface plasmon polaritons," *IEEE Trans. Ant. and Prop.*, Vol. 66, No. 12, 7111–7116, 2018.
103. Wang, M., H. F. Ma, H. C. Zhang, et al., "Frequency-fixed beam-scanning leaky-wave antenna using electronically controllable corrugated microstrip line," *IEEE Trans. Ant. and Prop.*, Vol. 66, No. 9, 4449–4457, 2018.
104. Feng, W. J., Y. H. Feng, W. C. Yang, et al., "High-performance filtering antenna using spoof surface plasmon polaritons," *IEEE Trans. Plasm. Sci.*, Vol. 47, No. 6, 2832–2837, 2019.
105. Zhang, X. F., J. Fan, and J. X. Chen, "High gain and high-efficiency millimeter-wave antenna based on spoof surface plasmon polaritons," *IEEE Trans. Ant. and Prop.*, Vol. 67, No. 1, 687–691, 2019.
106. Lu, J. Y., H. C. Zhang, P. H. He, et al., "Design of miniaturized antenna using corrugated microstrip," *IEEE Trans. Ant. and Prop.*, Vol. 68, No. 3, 1918–1924, 2020.

107. Liu, L. L., Z. Li, C. Q. Gu, et al., "Smooth bridge between guided waves and spoof surface plasmon polaritons," *Opt. Lett.*, Vol. 40, No. 8, 1810–1813, 2015.
108. Liu, L. L., Z. Li, B. Z. Xu, et al., "High-efficiency transition between rectangular waveguide and domino plasmonic waveguide," *AIP Adv.*, Vol. 5, 027105, 2015.
109. Liu, L. L., Z. Li, B. Z. Xu, et al., "A high-efficiency rectangular waveguide to Domino plasmonic waveguide converter in X-band," *Proc. 3rd Asia-Pacific Conf. Ant. and Prop.*, 974–977, 2014.
110. Guan, D. F., P. You, Q. F. Zhang, et al., "Hybrid spoof surface plasmon polariton and substrate integrated waveguide transmission line and its application in filter," *IEEE Trans. Micro. Theory and Tech.*, Vol. 65, No. 12, 4925–4932, 2017.
111. Guan, D. F., P. You, Q. F. Zhang, et al., "Slow-wave half-mode substrate integrated waveguide using spoof surface plasmon polariton structure," *IEEE Trans. Micro. Theory and Tech.*, Vol. 66, No. 6, 2946–2952, 2018.
112. Liu, L. L., L. Ran, H. D. Guo, X. Chen, and Z. Li, "Broadband plasmonic circuitry enabled by channel domino spoof plasmons," *Progress In Electromagnetic Research*, Vol. 164, 109–118, 2019.
113. Liu, L. L., L. Wu, J. J. Zhang, et al., "Backward phase matching for second harmonic generation in negative-index conformal surface plasmonic metamaterials," *Adv. Sci.*, 1800661, 2018.
114. Gao, X. X., J. J. Zhang, H. C. Zhang, et al., "Dynamic controls of second-harmonic generations in both forward and backward modes using reconfigurable plasmonic metawaveguide," *Adv. Opt. Mater.*, 1902058(1-8), 2020.
115. Zhang, H. C., T. J. Cui, J. Xu, et al., "Real-time controls of designer surface plasmon polaritons using programmable plasmonic metamaterial," *Adv. Mater. Technol.*, Vol. 2, 1600202, 2016.
116. Wang, M., H. F. Ma, W. X. Tang, et al., "Programmable controls of multiple modes of spoof surface plasmon polaritons to reach reconfigurable plasmonic devices," *Adv. Mater. Technol.*, Vol. 4, 1800603, 2019.
117. Zhang, H. C., T. J. Cui, Y. Luo, et al., "Active digital spoof plasmonics," *Nat. Sci. Rev.*, Vol. 7, 261–269, 2020.
118. Zhang, H. C., S. Liu, X. P. Shen, et al., "Broadband amplification of spoof surface plasmon polaritons at microwave frequencies," *Laser Photon. Rev.*, Vol. 9, No. 1, 83–90, 2015.
119. Gao, X. X., J. J. Zhang, and Y. Luo, "Reconfigurable parametric amplifications of spoof surface plasmons," *Adv. Sci.*, Vol. 8, 2100795, 2021.
120. Wan, X., J. Y. Yin, H. C. Zhang, and T. J. Cui, "Dynamic excitation of spoof surface plasmon polaritons," *Appl. Phys. Lett.*, Vol. 105, No. 8, 2014.
121. Zhang, H. C., Y. Fan, J. Guo, et al., "Second-harmonic generation of spoof surface plasmon polaritons using nonlinear plasmonic metamaterials," *ACS Photon.*, Vol. 3, No. 1, 139–146, 2016.
122. Zhang, X. R., W. X. Tang, H. C. Zhang, et al., "A spoof surface plasmon transmission line loaded with varactors and short-circuit stubs and its application in Wilkinson power dividers," *Adv. Mater. Technol.*, Vol. 3, 1800046, 2018.
123. Zhang, L. P., H. C. Zhang, M. Tang, et al., "Integrated multi-scheme digital modulations of spoof surface plasmon polaritons," *SCI. China Inf. Sci.*, Vol. 63, No. 202302, 1–10, 2020.
124. Zhang, H. C., L. P. Zhang, P. H. He, et al., "A plasmonic route for the integrated wireless communication of subdiffraction-limited signals," *Light Sci. & Appl.*, Vol. 9, 113, 2020.
125. Kreibig, U. and M. Vollmer, *Optical Properties of Metal Clusters*, Springer, Berlin, 1995.
126. Garcia-Vidal, F. J. and J. B. Pendry, "Collective theory for surface-enhanced Raman scattering," *Phys. Rev. Lett.*, Vol. 77, 1163, 1996.
127. Atwater, H. A. and A. Polman, "Plasmonics for improved photovoltaic devices," *Nature Mater.*, Vol. 9, 205, 2010.
128. Pors, A., E. Moreno, L. Martín-Moreno, et al., "Localized spoof plasmons arise while texturing closed surfaces," *Phys. Rev. Lett.*, Vol. 108, No. 22, 223905, 2012.
129. Shen, X. P. and T. J. Cui, "Ultrathin plasmonic metamaterial for spoof localized surface plasmons," *Laser Photon. Rev.*, Vol. 8, No. 1, 137–145, 2014.

130. Wu, H. W., Y. Z. Han, H. J. Chen, et al., "Physical mechanism of order between electric and magnetic dipoles in spoof plasmonic structures," *Opt. Let.*, Vol. 42, No. 21, 4521–4524, 2017.
131. Huidobro, P. A., X. P. Shen, J. Cuerda, et al., "Magnetic localized surface plasmons," *Phys. Rev. X*, Vol. 4, No. 2, 021003, 2014.
132. Liao, Z., A. I. Fernández-Domínguez, J. J. Zhang, et al., "Homogenous metamaterial description of localized spoof plasmons in spiral geometries," *ACS Photon.*, Vol. 3, 1768–1775, 2016.
133. Li, Z., B. Z. Xu, C. Q. Gu, et al., "Localized spoof plasmons in closed textured cavities," *Appl. Phys. Lett.*, Vol. 104, 251601, 2014.
134. Li, Z., L. L. Liu, C. Q. Gu, et al., "Multi-band localized spoof plasmons with texturing closed surfaces," *Appl. Phys. Lett.*, Vol. 104, 101603, 2014.
135. Xu, B. Z., Z. Li, C. Q. Gu, et al., "Multi-band localized spoof plasmons in closed textured cavities," *Appl. Opt.*, Vol. 53, No. 30, 6950–6953, 2014.
136. Yang, B. J., Y. J. Zhou, and Q. X. Xiao, "Spoof localized surface plasmons in corrugated ring structures excited by microstrip line," *Opt. Express*, Vol. 23, No. 16, 21434, 2015.
137. Zhou, Y. J., Q. X. Xiao, and B. J. Yang, "Spoof localized surface plasmons on ultrathin textured MIM ring resonator with enhanced resonances," *Sci. Rep.*, Vol. 5, 14819, 2015.
138. Gao, Z., F. Gao, H. Y. Xu, et al., "Localized spoof surface plasmons in textured open metal surfaces," *Opt. Lett.*, Vol. 41, No. 10, 3–6, 2016.
139. Wu, H. W., H. J. Chen, H. Y. Fan, et al., "Trapped spoof surface plasmons with structured defects in textured closed surfaces," *Opt. Lett.*, Vol. 42, No. 4, 791–794, 2017.
140. Liao, Z., Y. Luo, A. I. Fernández-Domínguez, et al., "High-order localized spoof surface plasmon resonances and experimental verifications," *Sci. Rep.*, Vol. 5, 9590, 2015.
141. Gao, F., Z. Gao, X. H. Shi, et al., "Dispersion-tunable designer-plasmonic resonator with enhanced high-order resonances," *Opt. Express*, Vol. 23, No. 5, 6896–902, 2015.
142. Xiao, Q. X., B. J. Yang, and Y. J. Zhou, "Spoof localized surface plasmons and Fano resonances excited by flared slot line," *J. Appl. Phys.*, Vol. 118, No. 23, 1–6, 2015.
143. Gao, Z., F. Gao, K. K. Shastri, and B. L. Zhang, "Frequency-selective propagation of localized spoof surface plasmons in a graded plasmonic resonator chain," *Sci. Rep.*, Vol. 6, 25576, 2016.
144. Gao, F., Z. Gao, Y. Luo, and B. L. Zhang, "Invisibility dips of near-field energy transport in a spoof plasmonic metadimer," *Adv. Fun. Mater.*, Vol. 26, 8307–8312, 2016.
145. Wu, H. W., Y. Li, H. J. Chen, et al., "Strong purcell effect for terahertz magnetic dipole emission with spoof plasmonic structure," *ACS Appl. Nano Mater.*, Vol. 2, 1045–1052, 2019.
146. Xu, B. Z., Z. Li, L. L. Liu, et al., "Non-concentric textured closed surface for huge local field enhancement," *J. Opt.*, Vol. 19, No. 1, 015005, 2016.
147. Huang, Y., J. J. Zhang, and T. J. Cui, "Revealing the physical mechanisms behind large field enhancement in hybrid spoof plasmonic systems," *J. Opt. Soc. Amer. B*, Vol. 35, No. 2, 396–401, 2018.
148. Gao, Z., F. Gao, Y. Zhang, et al., "Experimental demonstration of high-order magnetic localized spoof surface plasmons," *Appl. Phys. Lett.*, Vol. 107, No. 4, 1–5, 2015.
149. Gao, Z., F. Gao, Y. Zhang, and B. L. Zhang, "Complementary structure for designer localized surface plasmons," *Appl. Phys. Lett.*, Vol. 107, No. 19, 191103, 2015.
150. Gao, Z., F. Gao, and B. L. Zhang, "High-order spoof localized surface plasmons supported on a complementary metallic spiral structure," *Sci. Rep.*, Vol. 6, 24447, 2016.
151. Gao, Z., F. Gao, Y. Zhang, and B. L. Zhang, "Deep-subwavelength magnetic coupling-dominant interaction among magnetic localized surface plasmons," *Phys. Rev. B*, Vol. 93, No. 19, 195410, 2016.
152. Zhang, J. J., Z. Liao, Y. Luo, et al., "Spoof plasmon hybridization," *Laser Photon. Rev.*, Vol. 11, No. 1, 1600191, 2017.
153. Wu, H. W., Chen H. J., Xu H. F., et al., "Tunable multiband directional electromagnetic scattering from spoof Mie resonant structure," *Sci. Rep.*, Vol. 8, No. 1, 1–8, 2018.

154. Wu, H. W., F. Yang, J. Q. Quan, et al., "Multifrequency superscattering with high factors from a deep-subwavelength spoof plasmonic structure," *Phys. Rev. B*, Vol. 100, No. 23, 235443, 2019.
155. Shen, X. P., B. C. Pan, J. Zhao, Y. Luo, and T. J. Cui, "A combined system for efficient excitation and capture of LSP resonances and flexible control of SPP transmissions," *ACS Photon.*, Vol. 2, No. 6, 738–743, 2015.
156. Li, Z., L. L. Liu, B. Z. Xu, et al., "High-contrast gratings based spoof surface plasmons," *Sci. Rep.*, Vol. 6, 21199, 2016.
157. Tretyakov, S., *Analytical Modeling in Applied Electromagnetics*, Artech House, 2003.
158. Liu, L. L., Z. Li, B. Z. Xu, et al., "Ultra-low loss high-contrast gratings based spoof surface plasmonic waveguide," *IEEE Trans. on Micro. Theory and Tech.*, Vol. 65, No. 6, 2008–2018, 2017.
159. Li, Z., B. Z. Xu, L. L. Liu, et al., "Localized spoof surface plasmons based on subwavelength closed high contrast gratings: Concept and microwave-regime realizations," *Sci. Rep.*, Vol. 6, 27158, 2016.
160. Giovampaola, C. D. and N. Engheta, "Plasmonics without negative dielectrics," *Phys. Rev. B*, Vol. 93, 195152, 2016.
161. Li, Z., L. L. Liu, H. Y. Sun, et al., "Effective surface plasmon polaritons induced by modal dispersion in a waveguide," *Phys. Rev. Appl.*, Vol. 7, No. 4, 044028, 2017.
162. Prudêncio, F. R., J. R. Costa, C. A. Fernandes, et al., "Experimental verification of 'waveguide' plasmonics," *New J. Phys.*, Vol. 19, 123017, 2017.
163. Li, Z., Y. H. Sun, K. Wang, et al., "Tuning the dispersion of effective surface plasmon polaritons with multilayer systems," *Opt. express*, Vol. 26, No. 4, 4686–4697, 2018.
164. Demetriadou, A. and J. B. Pendry, "Taming spatial dispersion in wire metamaterial," *J. Phys.: Condens. Matter*, Vol. 20, 295222, 2008.
165. Luukkonen, O., M. G. Silveirinha, A. B. Yakovlev, et al., "Effects of spatial dispersion on reflection from mushroom-type artificial impedance surfaces," *IEEE Trans. on Micro. Theory and Tech.*, Vol. 57, No. 11, 2692–2699, 2009.
166. Wang, K., Z. Li, J. F. Shi, et al., "Broadband electromagnetic waves harvesting based on effective surface plasmon polaritons," *Cross-Strait Quad-Regional Radio Science and Wireless Technology Conference (CSQRWC)*, 21–24, 2018.
167. Li, Z., Y. H. Sun, and H. Y. Sun, "Spoof surface plasmons tunneling through an epsilon-near-zero material channel," *J. Phys. D: Appl. Phys.*, Vol. 50, 375105 (7pp), 2017.
168. Huang, T. J., J. Zhao, L. Z. Yin, and P. K. Liu, "Terahertz subwavelength edge detection basedon dispersion-induced plasmons," *Opt. Lett.*, Vol. 46, No. 11, 2746–2749, 2021.
169. Yin, L. Z., F. Y. Han, J. Zhao, et al., "Constructing hyperbolic metamaterials with arbitrary medium," *ACS Photon.*, Vol. 8, 1085–1096, 2021.
170. Huang, T. J., L. Z. Yin, J. Zhao, et al., "Amplifying evanescent waves by dispersion-induced plasmons: Defying the materials limitation of the superlens," *ACS Photon.*, Vol. 7, 2173–2181, 2020.
171. Yang, Z. B., D. F. Guan, P. You, et al., "Compact effective surface plasmonpolariton frequency splitter basedon substrate integrated waveguide," *J. Phys. D: Appl. Phys.*, Vol. 52, 435103 (7pp), 2019.
172. Sakotic, Z., M. Drljaca, G. Kitic, et al., "LTCC dual-band bandpass filter based on SPP like propagation in substrate integrated waveguide," *IEEE Eurocon International Conference on Smart Technologies*, 1–4, July 2019.
173. Zhang, A. Q., W. B. Lu, Z. G. Liu, and Y. Li, "Deeper confinement of electromagnetic waves beyond spoof surface plasmon polaritons," *IEEE Trans. Ant. and Prop.*, Vol. 69, No. 4, 2142–2150, 2021.
174. Shi, J. F., Z. Li, L. L. Liu, et al., "Lateral dimension tuned ultra-low loss effective surface plasmonic waveguide," *J. Phys. D: Appl. Phys.*, Vol. 52, No. 2019, 105101 (7pp), 2019.

175. Li, Z., L. L. Liu, A. I. Fernández-Domínguez, et al., "Mimicking localized surface plasmons with structural dispersion," *Adv. Optical Mater.*, Vol. 7, No. 10, 1970036, 2019.
176. Li, W. Q. and Y. J. Zhou, "Effective localized surface plasmons resonator excited by substrate integrated waveguide," *IEEE MTT-S International Microwave Workshop Series on Advanced Materials and Processes for RF and THz Applications*, 9199740, 2020.
177. Yu, Y. R., L. L. Liu, Q. Jiang, et al., "Ultracompact effective localized surface plasmonic bandpass filter for 5G applications," *IEEE Trans. Micro. Theory and Tech.*, Vol. 69, No. 4, 2220–2228, 2021.
178. Ji, Y. L., Z. Li, J. F. Shi, et al., "A miniaturized dual-mode cavity filter based on effective localized surface plasmons," *IEEE Inter. Conf. on Com. Electro.*, 8779023, 2019.
179. Jiang, Q., Y. Q. Yu, Y. F. Zhao, et al., "Ultra-compact effective localized surface plasmonic sensor for permittivity measurement of aqueous ethanol solution with high sensitivity," *IEEE Trans. on Inst. and Meas.*, Vol. 70, 6008709, 2021.
180. Pendry, J. B., A. I. Fernandez-Dominguez, Y. Luo, and R. K. Zhao, "Capturing photons with transformation optics," *Nat. Phys.*, Vol. 9, 518, 2013.
181. Pendry, J. B., P. A. Huidobro, Y. Luo, and E. Galiffi, "Compacted dimensions and singular plasmonic surfaces," *Science*, Vol. 358, 915, 2017.
182. Yang, F., P. A. Huidobro, and J. B. Pendry, "Transformation optics approach to singular metasurfaces," *Phys. Rev. B*, Vol. 98, 125409, 2018.
183. Yves, S., R. Fleury, T. Berthelot, et al., "Crystalline metamaterials for topological properties at subwavelength scales," *Nat. Comm.*, Vol. 8, 16023, 2017.
184. Liu, W. and Y. S. Kivshar, "Generalized Kerker effects in nanophotonics and meta-optics," *Opt. Express*, Vol. 26, No. 10, 13085–13105, 2018.
185. Liu, W., A. E. Miroshnichenko, D. N. Neshev, and Y. S. Kivshar, "Broadband unidirectional scattering by magneto-electric core-shell nanoparticles," *ACS Nano*, Vol. 6, No. 6, 5489–5497, 2012.
186. Liu, W., A. E. Miroshnichenko, R. F. Oulton, et al., "Scattering of core-shell nanowires with the interference of electric and magnetic resonances," *Opt. Lett.*, Vol. 38, No. 14, 2621–2624, 2013.
187. Poutrina, E., A. Rose, D. Brown, et al., "Forward and backward unidirectional scattering from plasmonic coupled wires," *Opt. Express*, 21, No. 25, 31138–31154, 2013.
188. Liu, L. L., Z. Li, C. Q. Gu, et al., "A corrugated perfect magnetic conductor surface supporting spoof surface magnon polaritons," *Opt. Express*, Vol. 22, No. 9, 10675–10681, 2014.
189. Ng, B. H., J. F. Wu, S. M. Hanham, et al., "Spoof plasmon surfaces: A novel platform for THz sensing," *Adv. Opt. Mat.*, Vol. 1, No. 543, 543–548, 2013.
190. Ng, B. H., S. M. Hanham, and J. F. Wu, "Broadband terahertz sensing on spoof plasmon surfaces," *ACS Photon.*, Vol. 1, No. 10, 1059–1067, 2014.
191. Ma, Z., S. M. Hanham, P. A. Huidobro, et al., "Terahertz particle-in-liquid sensing with spoof surface plasmon polariton waveguides," *APL Photon.*, Vol. 11, No. 2, 116102, 2017.
192. Zhou, J., L. Chen, Q. Y. Sun, et al., "Terahertz on-chip sensing by exciting higher radial order spoof localized surface plasmons," *Appl. Phys. Express*, Vol. 13, 012014, 2020.
193. Chen, W., Ş. Kaya Özdemir, and G. Zhao, "Exceptional points enhance sensing in an optical microcavity," *Nature*, Vol. 548, 192–198, 2017.
194. Chang-Hasnain, C. J., Y. Zhou, M. C. Y. Huang, et al., "High-contrast grating VCSELs," *IEEE J. Sel. Top. Quan. Electro.*, Vol. 15, No. 3, 869–878, 2009.
195. Mateus, C. F. R., M. C. Y. Huang, Y. Deng, et al., "Ultrabroadband mirror using low-index cladded subwavelength grating," *IEEE Photon. Technol. Lett.*, Vol. 16, 518–520, 2004.
196. Zhou, Y., M. C. Y. Huang, C. Chase, et al., "High-index-contrast grating (HCG) and its applications in optoelectronic devices," *IEEE J. Sel. Top. Quantum Electron.*, Vol. 15, 1485–1499, 2009.
197. Xu, H. N. and Y. C. Shi, "Silicon-waveguide-integrated high-quality metagrating supporting bound state in the continuum," *Laser Photon. Rev.*, Vol. 14, 1900430 (6pp), 2020.

198. Fattal, D., J. Li, Z. Peng, et al., "Flat dielectric grating reflectors with focusing abilities," *Nature Photonics*, Vol. 4, 466–470, 2010.
199. Chang-Hasnain, C. J., "High-contrast gratings as a new platform for integrated optoelectronics," *Semicond. Sci. Technol.*, Vol. 26, 014043 (11pp), 2011.
200. Chang-Hasnain, C. J. and W. J. Yang, "High-contrast gratings for integrated optoelectronics," *Adv. Opt. and Photon.*, Vol. 4, 379–440, 2012.
201. Yang, W. J. and C. J. Chang-Hasnain, "Physics of high contrast gratings: A band diagram insight," *Proc. SPIE*, Vol. 8633, 863303, High Contrast Metastructures II, 2013.
202. Li, Y., I. Liberal, C. D. Giovampaola, and N. Engheta, "Waveguide metatronics: Lumped circuitry based on structural dispersion," *Sci. Adv.*, Vol. 2, e1501790, 2016.
203. Park, J. H., Y. H. Ryu, and J. G. Lee, "Epsilon negative zeroth-order resonator antenna," *IEEE Trans. Ant. and Prop.*, Vol. 55, No. 12, 3710–3712, 2007.
204. Niu, X. X., X. Y. Hu, S. S. Chu, and Q. H. Gong, "Epsilon-near-zero photonics: A new platform for integrated devices," *Adv. Opt. Mater.*, Vol. 6, 1701292, 2018.
205. Liberal, I., A. M. Mahmoud, Y. Li, et al., "Photonic doping of epsilon-near-zero media," *Science*, Vol. 355, No. 6329, 1058–1062, 2017.
206. Cai, W. and V. M. Shalaev, *Optical Metamaterials: Fundamentals and Applications*, Springer, New York, 2010.
207. Pendry, J. B., "Negative refraction makes a perfect lens," *Phys. Rev. Lett.*, Vol. 85, 3966, 2000.
208. Stone, M., "Gravitational anomalies and thermal Hall effect in topological insulators," *Phys. Rev. B*, Vol. 85, 184503, 2012.
209. Lundeberg, M. B., Y. D. Gao, R. Asgari, et al., "Tuning quantum nonlocal effects in graphene plasmonics," *Science*, Vol. 357, No. 6347, 187–191, 2017.
210. Raza, S., S. I. Bozhevolnyi, and M. Wubs, "Nonlocal optical response in metallic nanostructures," *J. Phys.: Condens. Matter*, Vol. 27, 183204 (17pp), 2015.
211. Prodan, E., C. Radloff, N. J. Halas, and P. Nordlander, "A hybridization model for the plasmon response of complex nanostructures," *Nature*, Vol. 302, No. 5644, 419–422, 2003.
212. Luo, Y., D. Y. Lei, S. A. Maier, and J. B. Pendry, "Broadband light harvesting nanostructures robust to edge bluntness," *Phys. Rev. Lett.*, Vol. 108, 023901, 2012.